Faculdade de Engenharia da Universidade do Porto

Universidade do Porto

Faculdade de Engenharia

FEUP

Dissertação de Mestrado

Mestrado em Engenharia Biomédica

Contributions to the segmentation of dermoscopic images

Pedro Miguel Martins Ferreira

Julho de 2012

Universidade do Porto

Faculdade de Engenharia

FEUP

Dissertação de Mestrado

Contributions to the segmentation of dermoscopic images

Autor: **Pedro Miguel Martins Ferreira (MEB09015)**

Orientadora: **Prof. Paula Rocha**
Co-Orientadora: **Prof. Teresa Mendonça**

*Tese submetida à Faculdade de Engenharia
da Universidade do Porto para obtenção do
grau de Mestre em Engenharia Biomédica*

Julho de 2012

Acknowledgments

I would like to thank both my supervisors, Prof. Paula Rocha and Prof. Teresa Mendonça, for their permanent support, guidance and availability. They were a great inspiration for me, giving me useful ideas and improving my knowledge during the development of this dissertation.

To Dr. Jorge Rozeira, Director of the Dermatology Service of the Hospital Pedro Hispano, many thanks for his precious help in providing the dermoscopic images and the manual segmentations used as ground truth to validate the results of this work.

A special thanks to my family, who always gave me the best conditions to study and to follow my dreams. It would not be possible to accomplish this work without their support, understanding, encouragement, and love.

Thanks to all my friends and classmates, for their friendship, and specially for every moment of entertainment and relaxation that they have shared with me.

Abstract

Melanoma is the most dangerous and deadly type of skin cancer. However, if it is diagnosed in an early stage there is a high probability of being cured. In this regard, several imaging techniques have been explored to improve the diagnosis accuracy of skin lesions. Dermoscopy is one of the most relevant of such diagnosis techniques, since it allows the *in vivo* observation and inspection of skin lesions, and hence a better visualization of their morphological structures.

Since the diagnosis accuracy of dermoscopy significantly depends on the experience of the dermatologists, and the visual interpretation and examination of this kind of images is time consuming, several computer-aided diagnosis systems have been introduced to assist the clinical diagnosis of dermatologists. Image segmentation is one of the most relevant tasks in these systems, since the accuracy of segmentation may determine their success or failure.

The availability and generation of manually segmented images performed by expert dermatologists, to be used as ground truth, is an essential aspect in the evaluation and validation of automatic segmentation methods. Herein, a novel annotation tool for manual segmentation of dermoscopic images is proposed. This tool, called DerMAT, allows building up a ground truth database with the manual segmentations both of pigmented skin lesions and of other regions of interest. The developed tool was set up based on the requirements and suggestions of dermatologists, and has been used and tested in clinical environment. Compared with other existing annotation tools, DerMAT presents some advantages with respect to others, namely better freehand drawing and reshaping functionalities.

Furthermore, different kinds of algorithms for the automatic segmentation of the skin lesion in dermoscopic images are implemented and evaluated. Some performance metrics are computed for the quantitative assessment of the segmentation results, using as ground truth a database of images manually segmented by an expert dermatologist. Among the implemented segmentation approaches, the GVF snake method achieves the best segmentation performance.

Keywords: Dermoscopy, image segmentation, ground truth

Resumo

O melanoma é a forma de cancro cutâneo mais agressiva e letal. No entanto, quando é diagnosticado numa fase ainda precoce e não invasiva, tem grande probabilidade de cura. Neste sentido, diversas técnicas de imagiologia têm sido exploradas para melhorar a precisão no diagnóstico de lesões cutâneas. A dermoscopia é uma das técnicas de diagnóstico mais importantes, uma vez que permite a observação e inspeção *in vivo* de lesões cutâneas, e assim uma melhor visualização das suas estruturas morfológicas.

Como a precisão do diagnóstico em dermoscopia depende significativamente da experiência dos dermatologistas e a interpretação deste tipo de imagens é uma tarefa demorada, vários sistemas de diagnóstico assistido por computador têm sido introduzidos para auxiliarem os dermatologistas. A segmentação de imagem é uma das tarefas mais importantes destes sistemas, uma vez que a precisão da segmentação determina o seu eventual sucesso ou insucesso.

A existência e criação de imagens segmentadas manualmente por dermatologistas, para serem utilizadas como referência, é um aspecto essencial na avaliação e validação dos métodos de segmentação automática. Deste modo, uma ferramenta de anotação para a segmentação manual de imagens dermatoscópicas é proposta neste trabalho. Esta ferramenta, denominada DerMAT, permite a construção de uma base de imagens de referência com as segmentações manuais tanto das lesões cutâneas como de outras regiões de interesse. A ferramenta desenvolvida foi criada com base nas sugestões e requesitos dos dermatologistas, tendo vindo a ser utilizada e testada por eles em ambiente clínico. Comparado com outras ferramentas de anotação existentes, o DerMAT apresenta algumas vantagens, nomeadamente melhores funcionalidades de segmentação manual e edição das segmentações.

Além disso, foram implementados e avaliados diferentes tipos de algoritmos para a segmentação automática da lesão cutânea em imagens dermatoscópicas. Para a avaliação quantitativa dos resultados da segmentação são determinadas algumas medidas de desempenho, usando como referência uma base de imagens segmentadas manualmente por um dermatologista experiente. Entre os métodos de segmentação implementados, o método "GVF snake" apresenta os melhores resultados.

Contents

List of Figures

List of Tables

Chapter 1

Introduction

1.1 Motivation

Skin cancer is one of the most frequent cancers among human beings. Malignant melanoma is the most aggressive and deadly type of skin cancer, and its incidence has been quickly increasing over the last years. In Portugal there are 10 000 new cases of skin cancer diagnosed each year, of which 1000 are malignant melanomas [1, 2].

The success of melanoma treatment depends directly on early diagnosis because, when detected in an early and non-invasive stage, the malignant melanoma can easily be excised with an excellent prognosis for the patient [3, 4].

In order to improve the accuracy of melanoma diagnosis various imaging techniques have been explored, including photography, dermoscopy, spectral imaging, LASER Doppler perfusion imaging, magnetic resonance imaging, and infrared thermal imaging [4]. Among these, dermoscopy is currently the most relevant imaging technique for melanoma diagnosis. Dermoscopy is a non-invasive diagnostic technique for the *in vivo* observation of pigmented skin lesions in a greater magnification, allowing a better visualization of their surface and subsurface structures. This is a very useful technique for the analysis of skin lesions and, when performed by experienced physicians, it has been shown to increase the diagnosis accuracy, specially of the melanoma [2, 5, 6].

Nevertheless, the visual interpretation and inspection of dermoscopic images is time consuming, subjective, and prone to bias even for trained dermatologists. Moreover, it was shown by Kittler *et al.* [7] that the diagnosis accuracy of dermoscopy significantly depends on the experience of the dermatologists, and when performed by untrained or less experienced physicians, dermoscopy was no better than clinical inspection with the unaided eye [7, 8].

Therefore, in the last few years, several computer-aided diagnosis systems of digital dermoscopic images have been introduced. An automatic dermoscopic image analysis system has

usually three stages, namely: image segmentation, feature extraction and selection, and lesion classification. The segmentation step is one of the most important ones, since a good segmentation is fundamental for subsequent classification, and also because some clinical features, such as asymmetry and border irregularity, can be directly obtained from the boundary of the lesion [9, 10]. Thus, the further investigation of automatic segmentation methods for dermoscopic images is of crucial importance.

The evaluation and validation of automatic segmentation methods requires a reliable ground truth database of manually segmented images. To our knowledge there is no available standard ground truth database of dermoscopic images that can be used by all the research community. As the ground truth databases have to be created manually by expert dermatologists, which is a quite cumbersome task, there is also a need for the development of graphical user interfaces/annotation tools that can support the manual segmentation of dermoscopic images, and this way make this task easier and practicable for dermatologists.

1.2 Aims

The purpose of this dissertation is twofold.

The first aim is the development of an annotation tool that supports the manual segmentation of dermoscopic images. This tool should allow building up a ground truth database with the manual segmentations both of pigmented skin lesions and of other regions of interest.

The second aim is the implementation and evaluation of different kinds of algorithms for the automatic segmentation of the pigmented skin lesion in dermoscopic images.

1.3 Contributions

In this dissertation, our efforts were targeted towards the manual segmentation/ground truth creation issue as well as to the implementation of fully automated algorithms for the segmentation of dermoscopic images. In this regard, the main contributions of this work can be summarized as follows:

- A completely new annotation tool for manual segmentation of dermoscopic images is presented. Besides the manual segmentation itself, this tool has other interesting functionalities, such as: boundary reshaping, region labeling, multi-user ground truth annotation and segmentation comparison;

- Several algorithms for the automatic segmentation of the pigmented skin lesion are applied and evaluated, including automatic thresholding, region growing, watershed, k-means, mean-shift, and gradient vector flow (GVF). For some of these algorithms adaptations were

made in order to improve their performance and/or make the segmentation process completely automatic;

- In the automatic thresholding, an algorithm for automatic detection of the number of significant histogram peaks is developed in order to classify the image histogram as unimodal or bimodal. Thus, according to each situation one of two distinct algorithms, either the triangle method or Otsu's method, is used;

- An algorithm for automatic seed region creation in order to make the region growing method fully automatic is developed and implemented. For a given image, the seed region creation and definition is based on the horizontal and vertical projections of the image;

- In the gradient vector flow method, an approach for automatic initialization is proposed and applied. The initial contour is automatically defined for each image, mainly based on the information obtained from the canny edge detector.

Part of the work presented in this dissertation was published in the papers [11, 12, 13].

1.4 State of the art

1.4.1 Annotation tools for manual segmentation and ground truth creation

A reliable ground truth image database is necessary for the evaluation of the automatic segmentation algorithms performance. The creation and construction of a ground truth image database is of crucial importance, specially in the dermoscopy field, due to the non-existence of a public ground truth database of dermoscopic images. This task must be performed by expert dermatologists who have to manually segment and annotate each dermoscopic image, which can be a quite cumbersome and time-consuming task. There are some available annotation tools or image processing software systems that can be used for manual ground truth annotation. However, there is no available customized tool for dermoscopy, and moreover most of the existing tools are not uniquely directed for the manual segmentation and annotation tasks, since they also include many other functionalities (automatic segmentation methods, image filters, image enhancement algorithms, etc). Therefore, we focused our research into the annotation tools or image software systems that support the manual segmentation, and hence can be used for ground truth creation (typically drawing the boundary of the desired objects in an image and labeling each segmented object). Some of such tools are: ImageJ [14], Labelme [15], and Annotor [16]. The main features and functionalities of these tools are described below.

ImageJ is a public domain image processing and analysis tool. Overall, ImageJ can be used to display, edit, process, analyze, save, and print images. It supports a wide number of standard image formats, including TIFF, GIF, JPEG, BMP, DICOM, FITS and "raw" images. Moreover, this tool incorporates many image processing methods, such as histogram and contrast manipulation, edge detection, some standard image filters (mean, median, etc.), and a wide range of automated image segmentation algorithms. With ImageJ it is possible to create/draw user-defined regions of interest within an image in order to perform the manual segmentation. The selection of the region of interest can be performed using rectangular, elliptical, polygonal, and freehand drawing tools. The created region of interest can be filtered, filled in, and several measurements can be obtained directly from each segmented region (for instance area, circularity, etc.). The regions of interest can be resized and reshaped, but only when obtained using rectangular or elliptical drawing tools [14, 17].

Labelme is a database and a web-based tool for image annotation and instant sharing of such annotations. The purpose of the Labelme project is to provide and build up a large image dataset with ground truth labels to be used by computer vision researchers. The online annotation tool allows users to draw the boundary of the objects in an image through a polygonal drawing tool. The segmentation is completed when the user closes the polygon along the object's boundary. Once the polygon is closed, it is possible to define a label for the segmented object. Afterwards, the annotation is added to the database and becomes available for immediate download [18, 19].

Annotor is a manual image annotation tool that can be used to create ground truth data (labeled images). Overall, this tool allows drawing polygons along the object boundaries in an image, and associating a class/label to each segmented polygon. Then, the annotations can be exported into different files (XML, PNG, and TXT) to be used as input for machine learning algorithms. The main output is a XML file, which contains a list of the segmented polygons defined by a color, a class, and the corresponding control points positions. Moreover, it is possible to generate cropped images (PNG images with transparent background) sorted by class, where each cropped image corresponds to a segmented polygon [16].

There are many other image processing and image analysis tools that could be used to manually segment and to trace a region of interest in an image, such as Endrov [20], Mango [21], and FreeSurfer [22]. However, as these tools are more directed towards the application of image processing algorithms, or to handle a specific type of medical imaging (for instance FreeSurfer is a brain imaging software), they are not considered or described in this work.

1.4.2   Segmentation methods for dermoscopic images

Dermoscopic images are a great challenge for segmentation algorithms, because there are a great diversity of lesion shapes, boundaries, and colors along with several skin types and textures.

In some images there is a low contrast and/or a smooth transition between the lesion and the surrounding skin. Moreover, dermoscopic images usually contain some intrinsic skin features such as hairs, black frames, skin lines, blood vessels, and air bubbles [9, 10]. Therefore, several segmentation algorithms have been suggested to overcome these difficulties. These segmentation algorithms can be roughly divided into four main groups, namely thresholding, region-based, edge/contour-based, and clustering-based methods.

A comprehensive survey of the methods applied to the segmentation of skin lesions in dermoscopic images is provided in [10], in which the pre-processing, segmentation, and post-processing steps involved in each method are described. The authors also give a particular attention to the evaluation of the segmentation results according to the most widely used performance metrics.

A thresholding segmentation method is described in [23], where the segmented skin lesion is obtained by a fully automated histogram-based thresholding technique in which the thresholding is performed in each of the three color planes. Another example of thresholding is presented in [24]. In this paper, an automated threshold fusion method for the segmentation of the skin lesion is proposed, since a single thresholding algorithm is hardly robust enough to work well in a wide variety of dermoscopic images. This method involves the fusion of four popular thresholding algorithms, namely Huang's algorithm [25], Kapur's algorithm [26], Kittler's algorithm [27], and Otsu's algorithm [28]. The results demonstrate that the fusion method has a better performance when compared to each individual method. Most recently, Humayun *et al.* [29] propose a multilevel thresholding algorithm which iteratively divides the image histogram into multiple classes with an optimized selection of the threshold values using Otsu's method.

Thresholding techniques have the advantages of being computationally simple and fast, and produce good results on images where there is good contrast between the lesion and the surrounding skin. However, in the dermoscopic images these methods generally produce inconsistent results, since in some images there is a low contrast and a smooth transition between the lesion and the skin, which leads the algorithm to fail [9, 30].

Several region-based methods have been used in the segmentation of dermoscopic images. Celebi *et al.* [31] suggest a modified version of the JSEG algorithm for the skin lesion segmentation. In this algorithm the segmentation process is divided into two independent phases: (i) a color quantization, and (ii) a multiscale region growing segmentation. Moreover, Celebi *et al.* [32] propose a color image segmentation technique based on region growing and merging, called statistical region merging algorithm (SRM). In this paper, SRM is compared with four state of the art automatic segmentation methods (orientation-sensitive fuzzy c-means, dermatologist-like tumor extraction algorithm, mean shift clustering, and the modified JSEG method), and it is shown that this algorithm achieves the best segmentation results. Another region-based segmentation method can be found in [33], where the flooding variant of the watershed algo-

rithm is implemented for the segmentation of dermoscopic images. The watershed algorithm uses an intensity-based topographical representation, in which the holes are punched at each regional minimum in the image, and then the topography is slowly flooded from the holes at each regional minimum to define different regions in the image [34].

Generally, region-based methods have difficulties when the pigmented skin lesions present a great variety of colors or textures along with different skin types and textures, which leads to oversegmentation [9, 31].

An example of an edge-based method can be found in [35], where the skin lesion is segmented either by the geodesic active contours model or the geodesic edge tracing approach. The deformable active contours or snakes are one of the most commonly used approaches to segment objects, particularly in medical images. This technique is based on deforming a curve towards the minimization of a given energy function [35]. In [36], the gradient vector flow (GVF) snakes method is used to find the border of skin lesions in dermoscopic images. Here, an automatic snake initialization method is introduced to make the skin lesion segmentation automatically. The GVF snake has some advantages over a traditional snake, such as its insensitivity to initialization and its ability to move into boundary concavities. In [37] the pigmented skin lesion is segmented using an improved snake model. The authors propose a new type of dynamic energy force for snakes which incorporates a mean shift field term within the standard GVF objective function. The experimental results show that their mean shift based GVF algorithm has a better segmentation performance than the classical GVF algorithm.

One of the main problems of the edge-based approaches applied to dermoscopic images is the existence of weak edges in some images, resulting from a smooth transition between the lesion and the skin. In these cases, the contour can pass over the weak edges. Another drawback of edge-based methods is the presence of noise points in the images, which can be derived from some image artifacts, such as hairs, air bubbles, and skin lines. The result can be the convergence of the contour to noise points and an incorrectly segmented skin lesion. Moreover, in these techniques a great number of parameters, which affect the contour's behavior and performance, must be validated [9, 36].

Clustering approaches are used in [38], [39], [40], [41] and [42] for the segmentation of dermoscopic images. Generally, these methods involve the partitioning of a feature space into homogeneous regions. In [38] the skin lesion is segmented using a modified version of the fuzzy c-means clustering technique that takes into account the cluster orientation. Gómez *et al.* [39] propose a contrast enhancement method based on independent histogram pursuit (IHP). The algorithm estimates a linear multispectral color space transformation that enhances the contrast between the lesion and the surrounding skin. Then, the skin lesion segmentation is performed using the *k*-means clustering technique. Melli *et al.* [40] compare the most spread color clus-

6

tering algorithms, namely median cut, k-means, fuzzy c-means and mean shift. According to the authors the best segmentation results are achieved by mean shift algorithm. The algorithm proposed in Zhou *et al.* [41] proceeds in a coarse-to-fine approach. First, the normalized cut algorithm is applied to a down-sampled version of the original image. Then, this segmentation result is adapted to the original image by using a histogram-based Bayesian classifier. Most recently, Devi *et al.* [42] suggest and compare several fuzzy based clustering techniques for skin lesion segmentation, including the fuzzy c-means algorithm, the possibilistic c-means algorithm, and the hierarchical c-means algorithm. According to their experimental results, the hierarchical c-means algorithm provides better performance when compared with the other two clustering algorithms.

The segmentation methods applied to dermoscopic images can also be divided into supervised and unsupervised methods. The supervised segmentation methods require user intervention, for instance in their initialization whereas unsupervised methods generally perform the segmentation without user interaction, or any kind of initialization. Moreover, unsupervised methods are preferred to ensure a reproducible result. However, user interaction is still required to correct an inadequate segmentation result [43].

Silveira *et al.* [9] propose and evaluate six different methods for dermoscopic image segmentation, including supervised and unsupervised segmentation methods, namely adaptive thresholding, gradient vector flow, adaptive snake, level set method of Chan *et al.* [44], expectation-maximization level set, and the fuzzy-based split-and-merge algorithm. They conclude that the best segmentation results are obtained by two supervised segmentation methods, more concretely by the adaptive snake and by the expectation-maximization level set methods. Fully automatic methods achieve slightly worse results.

It is important to note that the segmentation results in dermoscopic images are tightly coupled to the pre-processing step. Generally, the pre-processing step can include a color space transformation, contrast enhancement, and artifact removal. Celebi *et al.* [10] provide a useful review, in which the most widely used methods as pre-processing are presented. Recently, Abbas *et al.* [45] propose an effective pre-processing stage, where some image artifacts such as specular reflection, dermoscopic gel, and intrinsic cutaneous features (hair, blood vessels, skin lines, and ruler markings) are removed by homomorphic filtering, weighted median filtering, and an exemplar-based inpainting scheme.

1.5 Outline of the dissertation

In Chapter 2 the dermoscopy technique is introduced. Furthermore, the most widely used diagnosis algorithms for the evaluation of the pigmented skin lesions are presented, such as: the

pattern analysis, the ABCD rule, the 7-point checklist, and the Menzies method.

Chapter 3 presents the developed annotation tool, DerMAT, for manual segmentation and ground truth creation of dermoscopic images. Herein, the main functionalities of this tool are described in detail. Moreover, a functional evaluation of DerMAT is presented based on a comparison with other state of the art tools that can be also used for ground truth generation.

A detailed presentation of the implemented segmentation methods for the automatic detection of the pigmented skin lesions is given in Chapter 4. Here, the pre-processing step that is applied to the images is first presented, followed by a description of the theoretical aspects as well as the implementation methodology of each segmentation method. Afterwards, three performance metrics are given for the quantitative assessment of the segmentation performance, using as ground truth a set of manually segmented images performed by an expert dermatologist.

Finally, conclusions and some topics for future work are presented in Chapter 5.

Chapter 2

Dermoscopy

2.1 Dermoscopy: the technique

Dermoscopy, also known as dermatoscopy or skin surface microscopy, is a non-invasive diagnosis technique for the *in vivo* observation of pigmented skin lesions, providing a better visualization of their morphological structures, which would otherwise not be visible by the unaided eye [2].

This technique involves the use of an optical instrument with a magnification ranging from 6x to 40x and even up to 100x. One of the most widely used instruments is the dermatoscope (Figure 2.1), in which a spherical and achromatic lens is paired with a bright halogen beam that falls on the cutaneous surface, providing intra- and sub-epidermal illumination. Generally, around $4 - 7\%$ of the light is reflected from the dry skin surface, limiting the visualization of deeper structures. In order to reduce the reflected light, an immersion fluid (oil, gel, water, etc) is placed at the interface between the epidermis and the dermatoscope, or as an alternative polarized light dermatoscopes are used. The optically magnified image of the skin surface and subsurface is then either visually inspected or captured by a computer for subsequent digital image analysis and examination at the computer screen [4, 5, 46].

Figure 2.1: Manual dermatoscope (Adapted from [2]).

Digital dermoscopy uses digital or digitized dermoscopic images. It allows the storage, retrieval, and follow-up of pigmented skin lesions. Moreover, some systems can support teledermoscopy, and may offer the possibility of computer-aided diagnosis in order to assist the clinical

9

evaluation by dermatologists [8].

2.2 Differential diagnosis of pigmented skin lesions

The differential diagnosis of pigmented skin lesions can be a challenging task even for trained dermatologists. Thence, the Board of the Consensus Net Meeting on Dermoscopy (CNMD) agreed on a two-step procedure for the classification of pigmented skin lesions (Figure 2.2) [4, 47].
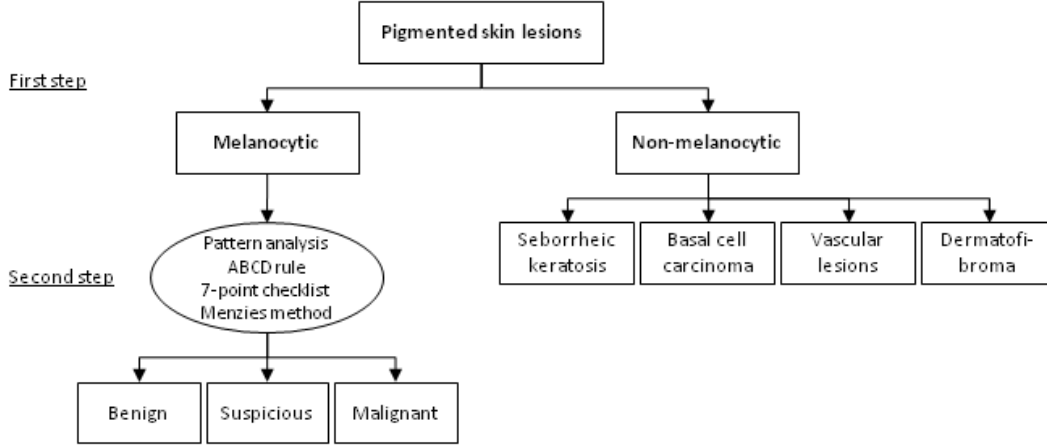
Figure 2.2: Two-step procedure for the differencial diagnosis of pigmented skin lesions (Adapted from [48]).

The purpose of the first step is to classify the lesion either as melanocytic or non-melanocytic. This decision is performed based on the presence of certain dermoscopic features, such as pigment network, globules, streaks, homogeneous blue pigmentation, and parallel pattern (Table 2.1). Overall, a pigmented skin lesion is considered as melanocytic when at least one of these criteria is present. Otherwise, the lesion should be one of the four main types of non-melanocytic lesions: seborrheic keratosis, basal cell carcinoma, vascular lesions, or dermatofibroma (this distinction is made based on another dermoscopic criteria) [48, 49].

Once the skin lesion is classified as melanocytic, the second step is to evaluate whether it is benign, suspicious, or malignant. Melanocytic lesions appear as a dark spot on the skin, resulting from an aggregation of the skin color pigment, called melanin, that is produced by a special type of cells, the melanocytes. The common melanocytic lesions are benign in nature (harmless), and usually called moles or melanocytic nevi. On the other hand, melanoma is a malignant type of melanocytic lesions, originating from an uncontrolled proliferation of melanocytes, that has the potential to metastasize [2, 4]. However, when melanoma is detected in a non-invasive, and early stage it can easily be treated and removed through a simple excision. Therefore, the early and correct diagnosis of melanocytic lesions is of crucial importance. In this regard, several diagnosis algorithms have been introduced in order to help differentiating between benign nevi and melanoma. The most widely used diagnosis algorithms are the pattern analysis, the ABCD

rule, the 7-point checklist, and the Menzies method. The ABCD rule and the 7-point checklist are semiquantitative models whereas Menzies method and pattern analysis are qualitative diagnosis models (these diagnosis methods are described in the following subsections) [2, 48, 49].

However, the diagnosis of melanocytic lesions is still a challenging task even using these diagnosis methods. Figure 2.3 shows some examples of melanocytic lesions, containing benign melanocytic nevi as well as melanomas. It demonstrates that sometimes melanomas and benign melanocytic lesions appear very similar. This could lead to one of the major problems in the diagnosis of melanocytic lesions, which is the underdiagnosis of a melanoma as being a benign lesion [2].
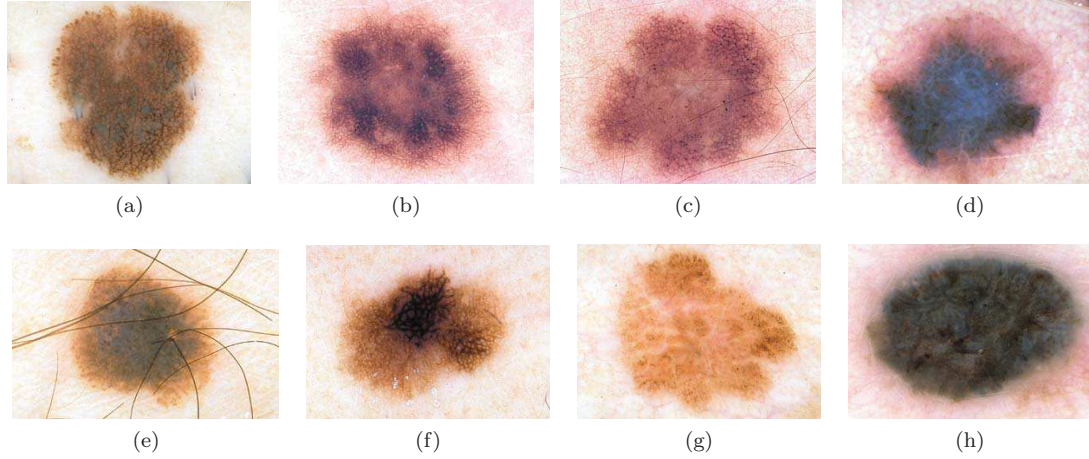
Figure 2.3: Examples of melanocytic lesions: (a-d) Benign melanocytic lesions; (e-h) Melanomas (Adapted from [2]).

2.2.1 Pattern analysis

Pattern analysis is the classical approach for diagnosing the pigmented skin lesions. This diagnosis procedure is based on a qualitative and simultaneous evaluation of several dermoscopic criteria. Therefore, the pigmented skin lesions are analyzed, in a first stage, with regard to their global pattern, and afterwards to their local pattern. Some of the most common global features that must be assessed are:

- **Reticular pattern:** these melanocytic lesions are composed almost entirely of a predominant pigment network.

- **Globular pattern:** characterized by the presence of numerous round to oval globules.

- **Cobblestone pattern:** it is a variant of globular pattern, which is characterized by the prevalence of closely, aggregated, large, angulated globules.

- **Starburst pattern:** characterized by the presence of radial streaks or globules regularly distributed around the periphery of the lesion.

11

- **Parallel pattern:** the parallel pattern is characterized by the presence of parallel pigmented lines.

Besides the global patterns, several local features have to be analyzed, such as: streaks, dots/globules, blue-whitish veil, regression structures, blotches, hypopigmented areas, and vascular patterns. These local dermoscopic structures are described in Table 2.1. Generally, the dermoscopic structures and colors are symmetrically distributed in benign lesions, whereas in melanomas these features are asymmetrically distributed and/or have an atypical shape [48, 49].

However, because of problems inherent to the reliability and reproducibility of the dermoscopic criteria used in pattern analysis, other diagnosis algorithms have been introduced in order to increase the accuracy, such as the ABCD rule, the 7-point checklist, and the Menzies method [2].

Table 2.1: Definition of some dermoscopic structures that are used in the diagnosis of melanocytic lesions (Adapted from [2, 50]).

Dermoscopic structure	Definition
Pigment network	Grid-like network consisting of pigmented lines (brown or black) and hypopigmented holes.
Dots/Globules	Spherical or oval, variously sized, black, brown or gray structures (dots are smaller than globules).
Streaks or Pseudopods	Brown-black, finger-like projections of the pigment network from the periphery of the lesion.
Blue-whitish veil	Confluent, opaque, irregular blue pigmentation with an overlying, white, ground-glass haze.
Regression structures	White scar-like depigmentation often combined with pepperlike areas (speckled blue-gray granules).
Blotches	Dark brown to black, usually homogeneous, areas of pigment obscuring underlying structures.
Hypopigmented areas	Localized or diffuse areas of decreased pigmentation within an otherwise ordinary pigmented lesion.
Vascular patterns	Vascular structures may include "comma vessels", "point vessels", "tree-like vessels", "wreath-like vessels", and "hairpin-like vessels".

2.2.2 ABCD Rule

The ABCD rule of dermatoscopy was introduced after pattern analysis in an attempt to simply the diagnosis process. This algorithm consists in a semiquantitative analysis of four different criteria of a given melanocytic lesion, including asymmetry (A), border (B), color (C), and differential structures (D) (Table 2.2). Each of these criteria is individually scored, based on how atypical they are identified in a lesion, and then multiplied by a given weight factor in order to

calculate the total dermatoscopy score (TDS) [2, 50]:

$$TDS = [(A_{score} \times 1.3) + (B_{score} \times 0.1) + (C_{score} \times 0.5) + (D_{score} \times 0.5)] \qquad (2.1)$$

The TDS ranges from 1 to 8.9. A lesion with a TDS value less than 4.75 can be considered as a benign melanocytic lesion. A lesion with a TDS value between 4.75 and 5.45 should be considered suspicious, and should either be excised or followed. Finally, a TDS value greater than 5.45 indicates that the lesion is highly suspicious of being a melanoma [2, 5, 50].

Table 2.2: ABCD rule of dermoscopy (Adapted from [2, 50]).

Criterion	Description	Score	Weight factor
Asymmetry	The lesion is divided by two orthogonal axes, and the asymmetry is assessed with regard to contour, colors, and structures (full symmetry - 0 points; asymmetry in one axis - 1 point; full asymmetry - 2 points).	0-2	1.3
Border	The lesion is divided into eight parts. Each eighth with an abrupt ending of pigment pattern at the periphery has a score of 1.	0-8	0.1
Color	1 point for the presence of each color (white, red, light-brown, dark-brown, blue-gray, black).	1-6	0.5
Differential structures	1 point for the presence of each structure (pigment network, structureless or homogeneous areas, streaks, dots, and globules).	1-5	0.5

In Figure 2.4 two examples of the application of the ABCD rule for diagnosing the melanocytic lesions are presented. The skin lesion in Figure 2.4(a) has a TDS value of 2.8, corresponding to a benign melanocytic lesion. Figure 2.4(b) contains a melanoma, which has a TDS value of 6.9.

(a)   (b)
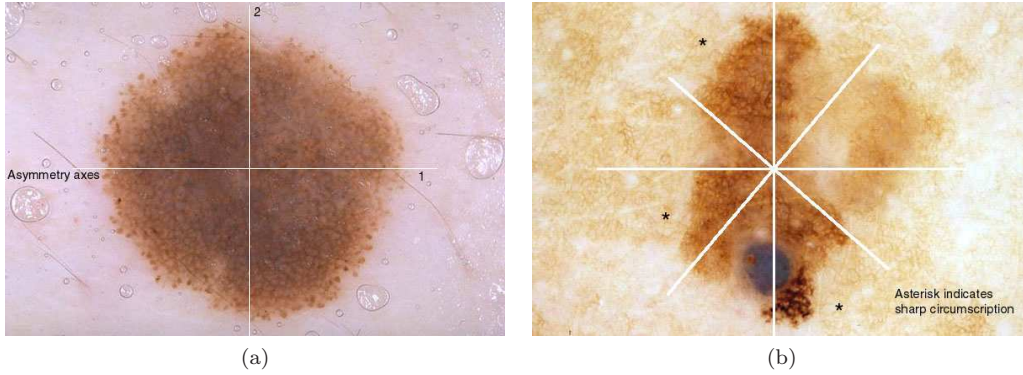
Figure 2.4: Differential diagnosis using the ABCD rule: (a) Benign skin lesion with a TDS value of 2.8 → Asymmetry: 0 × 1.3=0; Border: 8 × 0.1=0.8; Color: 2 (light-brown, dark-brown) × 0.5=1; Differential structures: 2 (network, globules) × 0.5=1; and (b) Melanoma with a TDS value of 6.9 → Asymmetry: 2 × 1.3=2.6; Border: 3* × 0.1=0.3; Color: 4 (light-brown, dark-brown, blue-gray, black) × 0.5=2; Differential structures: 4 (network, homogeneous areas, streaks, globules) × 0.5=2 (Adapted from [2]).

2.2.3 7-point checklist

The 7-point checklist is another semiquantitave approach that can be used for the diagnosis of melanocytic lesions. There are fewer dermoscopic features to analyze than in pattern analysis, and its scoring system is simpler than the one used in the ABCD rule of dermatoscopy.

In this algorithm, only seven dermoscopic features have to be assessed, which are divided into major and minor criteria (Table 2.3). Each major criterion identified in a given lesion receives 2 points, whereas each minor criterion receives only 1 point. Afterwards, the total score is computed by a simple addition of each individual score. If the total score is less than 3, the lesion is considered to be benign, but a lesion with a total score of 3 or greater has a high probability of being a melanoma [5, 47, 50].

Table 2.3: 7-Point Checklist (Adapted from [2]).

Criteria	7-Point score
Major criteria:	
1. Atypical pigment network	2
2. Blue-whitish veil	2
3. Atypical vascular pattern	2
Minor criteria:	
4. Irregular streaks	1
5. Irregular pigmentation	1
6. Irregular dots/globules	1
7. Regression structures	1

Figure 2.5 shows two examples of diagnosis using the 7-point point checklist. The pigmented skin lesion in Figure 2.5(a) corresponds to a melanoma, in which five dermoscopic characteristics can be identified, corresponding to a total score of 7. Figure 2.5(b) contains a Clark nevus, where only one dermoscopic characteristic is identified which corresponds to a score of 1.
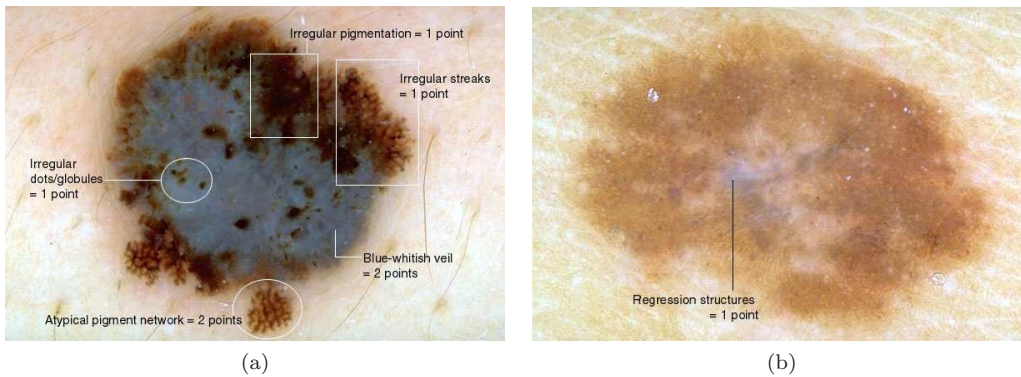
Figure 2.5: Differential diagnosis using the 7-point checklist: (a) Melanoma with a total score of 7; (b) Clark nevus with a total score of 1 (Adapted from [2]).

2.2.4 Menzies method

Menzies method is a qualitative diagnosis model like pattern analysis, and it is another attempt to simplify the assessment and analysis of the features present in dermoscopic images. According to this method, eleven dermoscopic features have to be assessed, which are divided in two main groups: negative and positive features. All of these dermoscopic features are scored as categorically present or absent, in order to reduce the observer errors that occur when criteria are graded [5, 50].

The negative features are the symmetry of pattern and the presence of a single color. Both of these criteria define a melanocytic lesion as benign. The symmetry of pattern can be defined as the symmetry of colors and/or structures observed in a lesion across all axes through the center of the lesion (it does not require symmetry of shape). The set of colors that are scored includes the black, gray, blue, red, dark brown, and tan. On the other hand, there are nine positive features, including the blue-whitish veil, multiple brown dots, pseudopods, radial streaming, scar-like depigmentation, peripheral black dots/globules, multiple colors (5-6), multiple blue/gray dots, and broad pigment network.

Therefore, a melanocytic lesion in which at least one of the nine positive features is present, added to the absence of both negative features is classified as a melanoma [2, 5].

Figure 2.6 illustrates two examples of the application of the Menzies method for diagnosing the melanocytic lesions. The skin lesion in Figure 2.6(a) is classified as a benign lesion, since it demonstrates symmetry of pattern across all axes drawn through the center of the lesion. Figure 2.6(b) contains a melanoma, since this lesion lacks symmetry of pattern, presents more than one color, and has two positive features (white scar-like areas and peripheral brown dots).

(a)   (b)
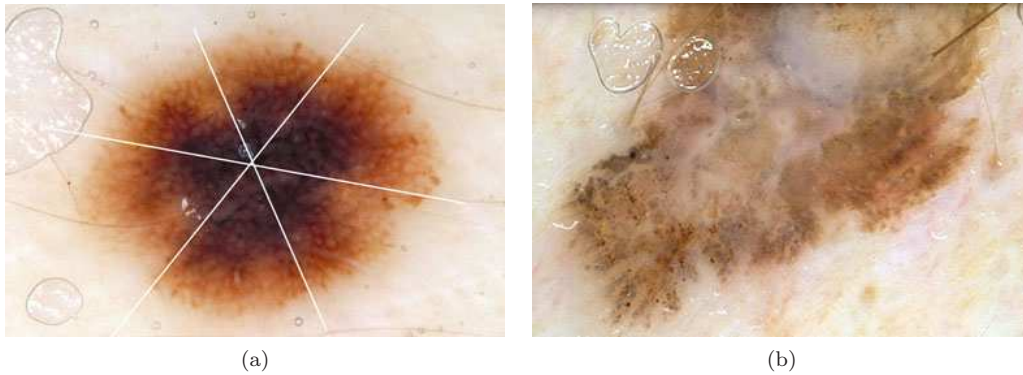
Figure 2.6: Differential diagnosis using the Menzies method: (a) Example of a benign melanocytic nevus; (b) Example of a melanoma (Adapted from [2]).

Chapter 3

DerMAT

The generation and collection of manually segmented images performed by expert dermatologists, to be used as ground truth, is an essential issue in the evaluation and validation of automatic segmentation methods.

In this chapter an annotation tool for manual segmentation of dermoscopic images, called DerMAT (**Der**moscopic images **M**anual **A**nnotation **T**ool), is presented. DerMAT allows building up a ground truth database with the manual segmentations both of pigmented skin lesions and of other regions of interest to be used in the assessment and validation of automatic segmentation and classification methods. This is a customized tool for dermoscopy, but it can easily be adapted to other medical imaging applications.

Therefore, in this chapter the main functionalities and features of DerMAT are first presented, followed by a functional comparison between DerMAT and other existing annotation tools.

3.1 DerMAT description

Overall, the developed tool allows drawing the boundary of the desired regions in an image, labeling each segmented region, and storing the result of segmentation. For this purpose, the user has a set of tools to be used sequentially to achieve the desired result. The main functionalities of DerMAT are as following:

   (i) Image upload and display;
  (ii) Manual segmentation (of the lesion or other regions of interest);
 (iii) Region labeling;
 (iv) Boundary reshaping;
  (v) *A posteriori* boundary edition;
 (vi) Multi-user ground truth annotation and segmentation comparison;
(vii) Storage of segmented images.
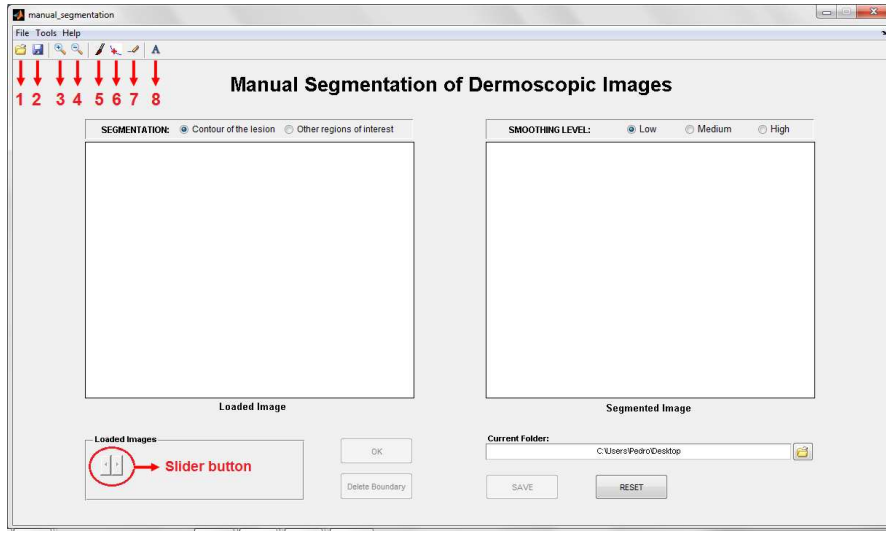
Figure 3.1: Initial aspect of the graphical user interface. **Toolbar Buttons:** 1-"Load Images"; 2-"Save as"; 3-"Zoom in"; 4-"Zoom out"; 5-"Manual segmentation"; 6-"Pointwise boundary reshaping"; 7-"Local boundary reshaping"; 8-"Region labeling".

The graphical user interface (GUI) of DerMAT was set up based on the requirements and suggestions of dermatologists and was implemented in a MATLAB environment (7.9.0 R2009b) taking into account its image processing toolbox and graphical facilities. Figure 3.1 shows the initial aspect of the GUI.

The developed tool has already been used by dermatologists at the Hospital Pedro Hispano for ground truth creation. More concretely, it was used in the scope of a task[1] within the project ADDI [51] for the manual segmentation of the color classes present in a set of 28 dermoscopic images. Furthermore, DerMAT has been used by non-clinical members of the project to perform the manual segmentation of the skin lesion in a dataset of 400 images, that are currently being validated by the expert dermatologists using this tool.

3.1.1   Image upload and display

With this application it is possible to load one image or several images at once. For this purpose, it is necessary to select the option "Load images" in the "File" menu, or simply press the button 1 on the toolbar (Figure 3.1).

Then a dialog box appears that enables the user to browse and select the image to be segmented. To load multiple images, simply press CTRL key and select the desired images (Figure 3.2). The loaded image is displayed on the left side of the interface. If several images have been loaded, the user can easily change the image that is being displayed through the slider button (Figure 3.1).

---

[1]C. S. P. Silva, A. R. S. Marcal, M. Pereira, T. Mendonça, and J. Rozeira, "Separability analysis of color classes on dermoscopic images," *ICIAR*, 2012.
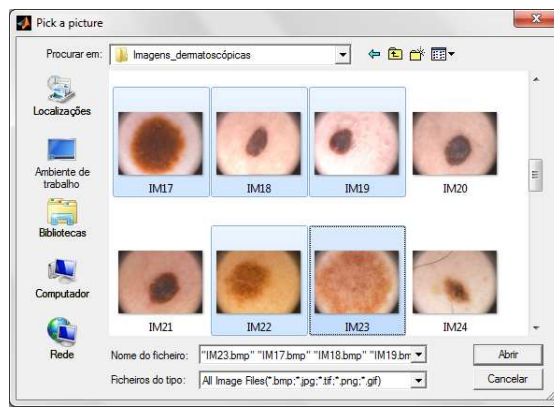
Figure 3.2: Dialog box that enables the user to browse and select the images to be segmented.

3.1.2 Manual segmentation

In order to perform the manual segmentation, this application allows to draw either single or multiple freehand regions of interest on the loaded image (using a pen tablet or a mouse). The user can choose between performing the manual segmentation of the lesion or other regions of interest through the radio buttons on the panel "Segmentation".

To achieve the manual segmentation it is necessary to select in the "Tools" menu the option "Manual Segmentation", or simply press the button 5 on the toolbar (Figure 3.1). Afterwards, the user must click and drag the pen tablet to draw the contour of the desired region.

When the user confirms the segmentation, the image with the final contour is displayed on the right side of the interface (Figure 3.3).
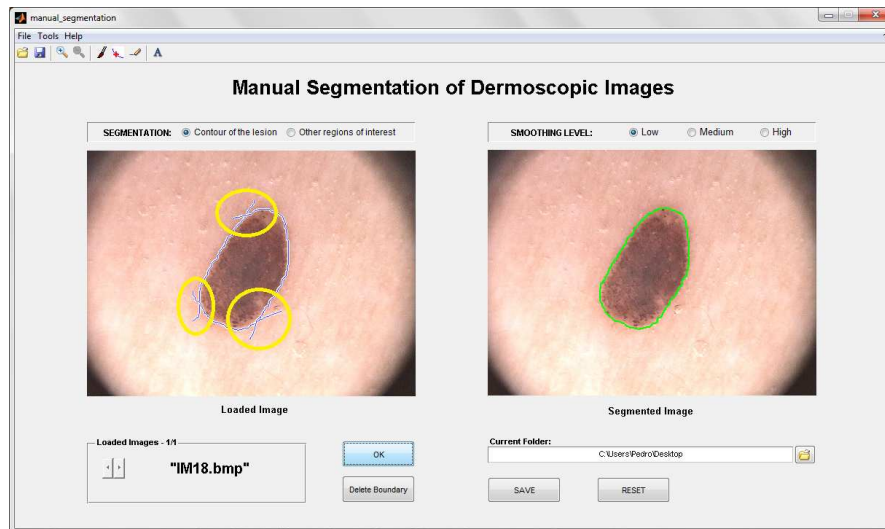
Figure 3.3: Manual segmentation: (Image on the left) Initial contour drawn by the user, with some undesirable extra lines (marked with circles); (Image on the right) Final contour after morphological filtering. Note that the final contour is smoother than the initial one and without undesirable extra lines.

It is important to note that the user can only confirm and complete the segmentation when a closed contour is drawn. When the user lifts the pen from the tablet before closing the contour,
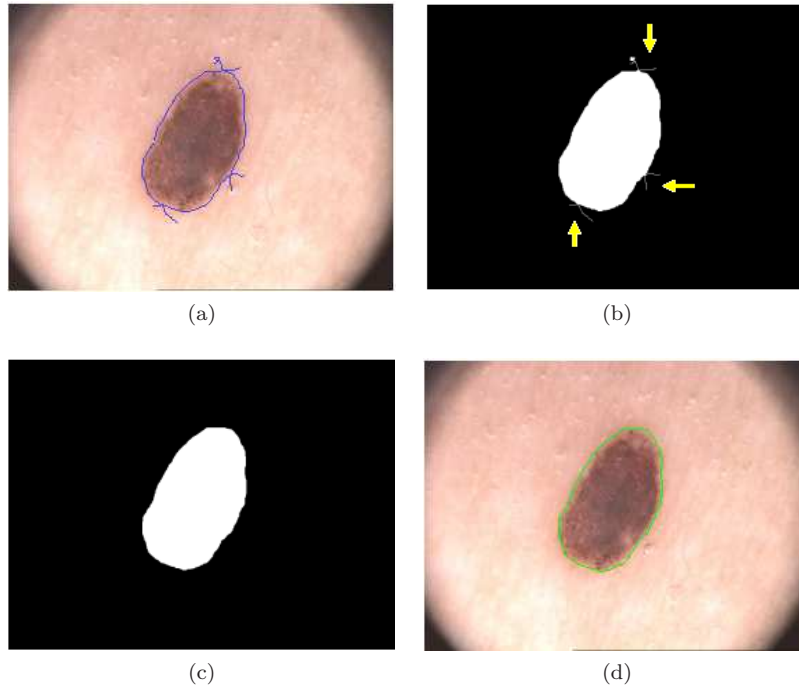
Figure 3.4: Morphological filtering: (a) Initial contour drawn by the user; (b) Binary mask of initial contour; (c) Binary image after morphological filtering; and (d) Final contour obtained from image "c".

the contour remains open. However, while the contour is open there is the possibility of resuming drawing until the user completes and closes the contour.

To our knowledge other available manual segmentation tools, such as ImageJ, do not have this possibility, since when the drawing is interrupted the contour is automatically closed with a straight line between the beginning and the end point. A functional comparison between DerMAT and other three state of the art softwares is presented in subsection 3.2.

To obtain the final contour from the initial one (drawn by user), a binary mask of the initial contour is first created, in which pixels with intensity value of 1 correspond to the segmented object, while pixels with value 0 correspond to the background. Then a morphological filtering is applied to this binary mask in order to smooth and remove extra lines that not belong to the contour. These lines may arise when the contour is drawn by means of multiple segments, specially at the points of intersection of these segments (Figures 3.3 and 3.4).

Basically, morphological filtering is divided into three stages (i) morphological erosion, (ii) selection of the biggest binary object from the image, and (iii) morphological dilation. The user has also the possibility to select the degree of smoothing of the morphological filter between low, medium and high. In each of these morphological operations a flat disk-shaped structuring element is used, with a specific radius for each smoothing level (low: radius 1; medium: radius 3; high: radius 7).

The manual segmentation of other regions of interest can be done in a very similar procedure to the manual segmentation of the lesion. For this purpose, the user must select the "Other
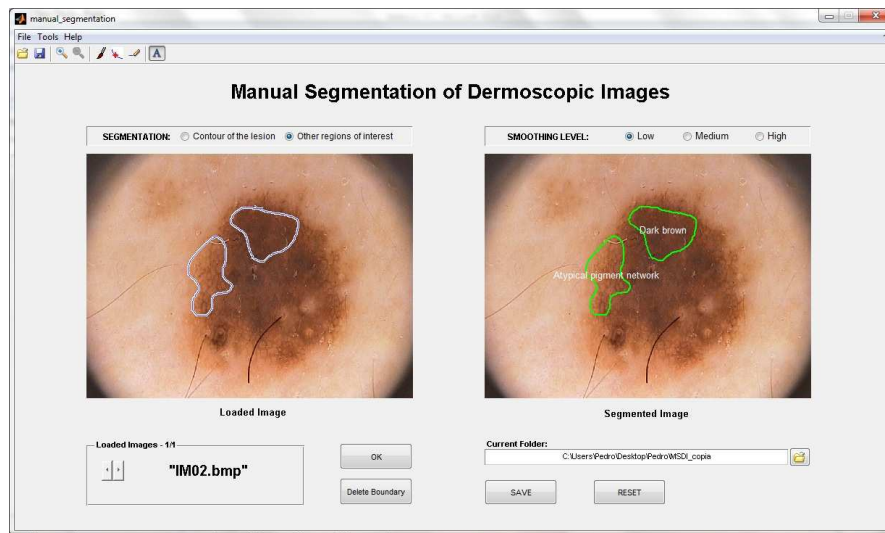
Figure 3.5: Segmentation example of other regions of interest with the respective labels.

regions of interest" radio button in the panel "Segmentation", and perform the segmentation of the desired regions in the same way as for the whole lesion. The contours of all segmented regions are shown simultaneously in the right window (Figure 3.5).

3.1.3 Region labeling

Another available functionality of this annotation tool is "Region labeling", which allows labeling the segmented regions. The user must select the option "Region labeling" in the "Tools" menu, or simply press the button 8 on the toolbar (Figure 3.1).
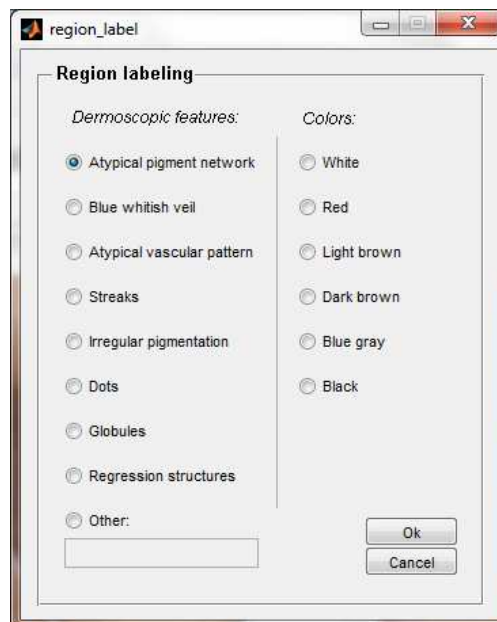
Figure 3.6: "Region labeling" window, in which there are several default labels that the user can select.

Afterwards, the user should move the pointer over the desired segmented region and click on

it. This produces another window where a number of default labels are available for selection. These labels include the main dermoscopic features and also the six typical colors that can be present in a dermoscopic lesion (Figure 3.6). The possibility of making a different annotation is also available. After selecting the desired label for each segmented region, the corresponding text annotation is placed inside the respective region (Figure 3.5).

3.1.4 Boundary reshaping

Even after finishing the manual segmentation it is possible to make some adjustments in the contour, if necessary. Two distinct methods were implemented to reshape the contour previously done, namely "Pointwise boundary reshaping" and "Local boundary reshaping".

3.1.4.1 Pointwise boundary reshaping

This method should be used to make small adjustments in the contour, because the reshaping is done point-by-point. For this, the user must select the option "Pointwise Boundary Reshaping" in the "Tools" menu, or simply press the button 6 on the toolbar (Figure 3.1). Forthwith the boundary turns red with some control points. From these points it is possible to change the shape of the contour. To accomplish this purpose, the user must click and drag the control points to their new positions (Figure 3.7).
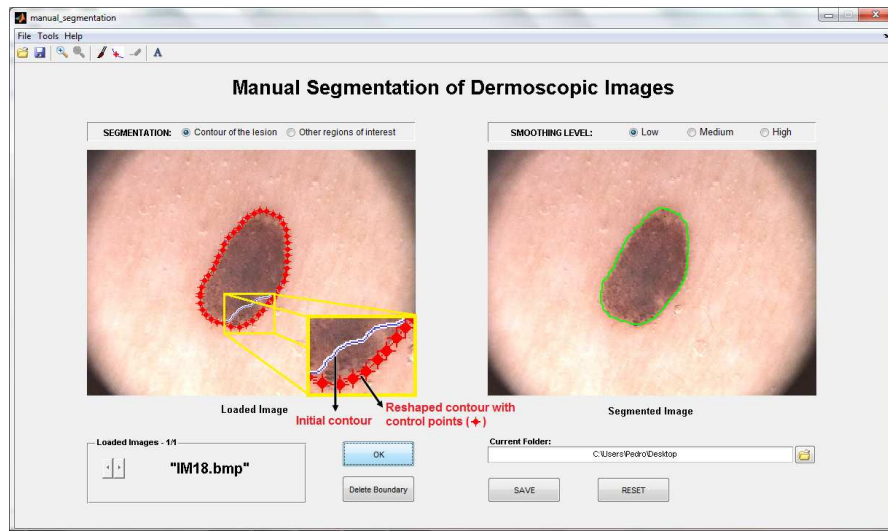
Figure 3.7: Pointwise boundary reshaping: (Image on the left) Initial contour (solid line) and the reshaped contour (red line with control points); (Image on the right) Final contour.

The interactive behaviors supported by this tool are described below:

- **Boundary reshaping:** Move the pointer over a control point. The pointer changes to a circle. Then, click and drag the control point to its new position.

- **Adding a new control point:** Move the pointer over the boundary and press the **A** key. Click the left mouse button to create a new control point at that position on the boundary.

22

- **Deleting a control point:** Move the pointer over a control point. The pointer changes to a circle. Then, click the right mouse button and select the option "Delete Vertex" from the context menu.

3.1.4.2 Local boundary reshaping

This method should be used when it is necessary to make great adjustments in the initial contour. For this purpose, the user must select the option "Local Boundary Reshaping" in the "Tools" menu, or simply press the button 7 on the toolbar (Figure 3.1).

Basically, this method allows the user to draw a line to define the new shape of the contour. The line must intersect the initial contour at least in two points to form a closed contour. This can be used to increase or reduce the size of the initial contour. Note that it is possible to increase and reduce the size of the contour with a single line (Figure 3.8).

(a)   (b)   (c)   (d)

(e)   (f)   (g)   (h)
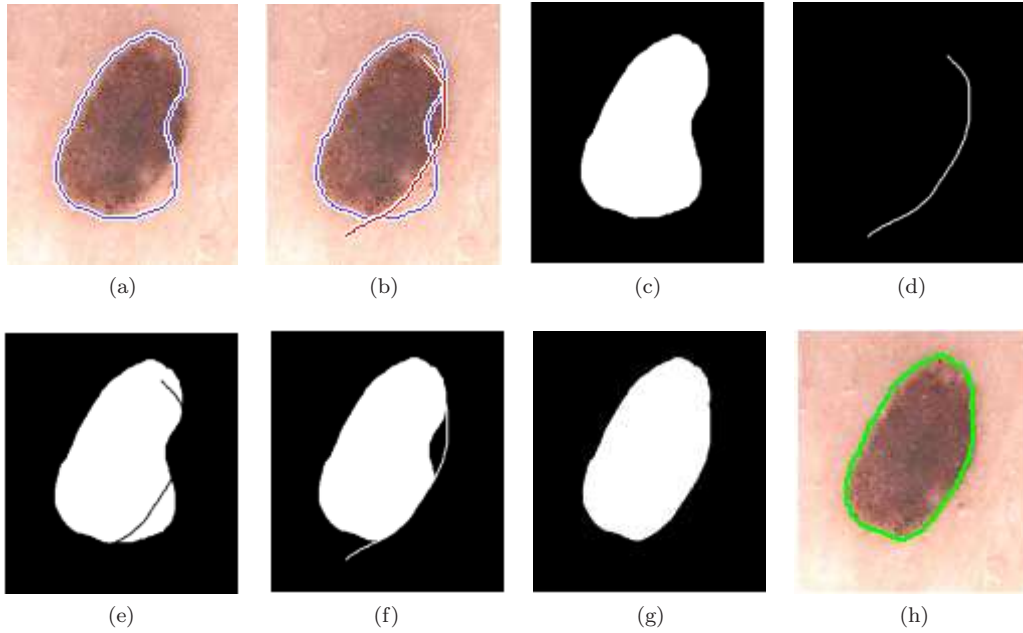
Figure 3.8: Local boundary reshaping: (a) Initial contour; (b) Initial contour and a new line to reshape the contour; (c)-(g) Intermediate steps; and (h) Final contour.

The final contour (Figure 3.8(h)) is obtained through a set of logical, arithmetical, and morphological operations:

(i) First, a binary image from the initial contour and another binary image from the new line are created (Figures 3.8(c) and 3.8(d) respectively);

(ii) Image subtraction between image (c) and (d) (Figure 3.8(e));

(iii) Selection of the biggest binary object from the image, and application of a logical OR operator between image (e) and (d) (Figure 3.8(f));

(iv) Application of a morphological filling in order to fill the image holes, and then a morphological open is used to remove the extra lines (Figure 3.8(g)).

3.1.5 *A posteriori* boundary edition

This functionality was implemented to be used as a way of speeding-up the ground truth creation task. It allows the visualization and the edition of a previously existing segmentation. In this way, segmentation may be performed in a first stage by less experienced (or even non medical) staff and then corrected by specialists. This can be used for medical training as well as for reducing the workload of the experts when building a ground truth database of large dimension.

Therefore, before starting the manual segmentation, the tool automatically searches in the current ground truth dataset if there exists a previously stored segmentation. In this case, the user can choose to visualize the previously existing contour and edit the border making use of the two existing boundary reshaping functionalities ("Pointwise boundary reshaping" and "Local boundary reshaping"). Otherwise, the user can discard the previous contour and perform a completely new manual segmentation.

3.1.6 Multi-user ground truth annotation and segmentation comparison

The manual segmentation of dermoscopic images is quite subjective and therefore it is desirable to collect segmentations performed by more than one dermatologist in order to create a reliable ground truth dataset [52]. In this regard, each user can set up and build his own manually segmented images dataset. Therefore, with this tool it is possible to collect annotations and segmentations of the same image by different users.

During the initialization of the tool the user can select an existing ground truth dataset (previously created by another user) or create his own new ground truth dataset (Figure 3.9).

Figure 3.9: Image dataset selection.

As each user is associated to one ground truth dataset, this tool is capable of making the comparison between segmentations of different users for the same image. To accomplish this purpose visual and quantitative comparisons are both presented. When this functionality is used for a given image another window is opened containing a list box with all datasets that have a segmentation of the current image for user selection. The user can compare his segmentation with the segmentations of one or more datasets (Figure 3.10).

For visual comparison the tool shows two or more segmentations superimposed on the same image. In addition, when only two segmentations are considered for comparison three performance metrics are given for the quantitative assessment of the segmentation discrepancies, namely the Hammoude distance, the false negative rate, and the false positive rate. These performance metrics are described in more detail in section 4.4.
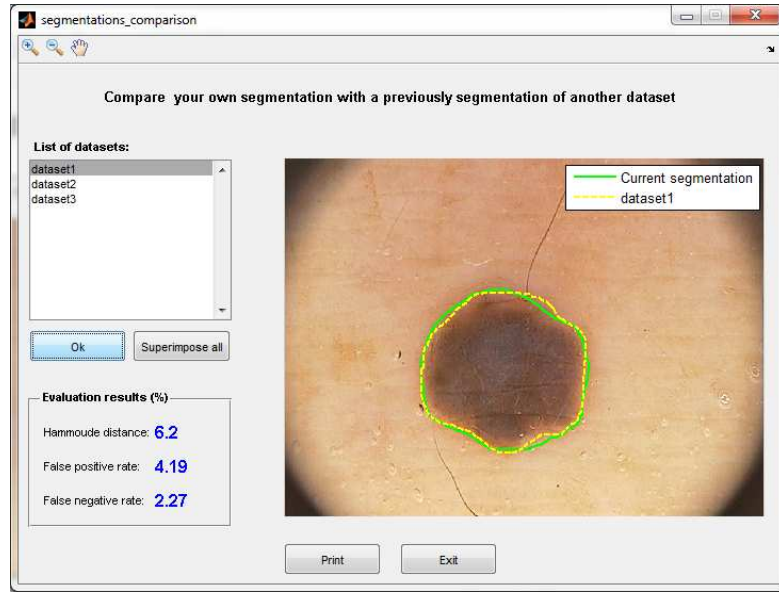
Figure 3.10: Segmentation comparison.

3.1.7 Storage of segmented images

Finally, this tool also allows storing the result of each manual segmentation. The ground truth dataset is created and organized automatically as the manual segmentations are stored. For each segmented image, a main folder with the same name of the image is created. In addition, two dedicated folders are created inside the main folder, one of them is for the storage of the manual segmentation of the lesion, and the other is for the storage of the manual segmentations of other regions of interest.

The segmentation result is saved as a binary image, where pixels with intensity value of 1 correspond to the segmented object, while pixels with value 0 correspond to the background. If different regions of interest were segmented, an individually binary image is created for each segmented region. Besides the binary image, a print of the original image with the contours of

all segmented regions and the respective labels is stored. This image is created and stored since it provides a suitable global information of the manual segmentation.

3.2   Functional evaluation of DerMAT

In this subsection a functional evaluation of DerMAT is presented based on a comparison with other available software systems that can be also used for manual image segmentation and ground truth generation, namely ImageJ, Labelme, and Annotor. The functional analysis and comparison was made using four different criteria. These criteria were defined based on the fundamental functionalities that an annotation tool for ground truth creation of dermoscopic images must support, including:

1. **Manual segmentation/drawing mode:** the manual segmentation of dermoscopic images has to be performed by a freehand drawing tool. The segmentation using polygonal selections is not precise enough in case of dermoscopic images, since skin lesions usually have complex shapes with quite irregular boundaries.

2. **Multiple ROI segmentation and labeling:** the annotation tool should support the segmentation and labeling of multiple ROIs in a given image, since besides the manual segmentation of the skin lesion it is also necessary to collect the manual segmentations of other regions of interest.

3. **Boundary reshaping:** after finishing the manual segmentation of a ROI it is sometimes necessary make some corrections in its boundary. Therefore, the annotation tool should allow reshaping the boundary of a segmented region without the necessity of redrawing it once again from the beginning.

4. **Output data generation:** the annotation tool should generate output data (with the boundary location and label of each segmented region) that can be easily used as an input in computer vision algorithms.

Table 3.1 summarizes the functional analysis of DerMAT according to the four different criteria. DerMAT and ImageJ are the only tools that comply with the first criterion (manual segmentation/drawing mode), since the other two applications only allow performing the manual segmentation through a polygonal selection tool. Although both DerMAT and ImageJ support a freehand manual segmentation, the freehand drawing tool supported by DerMAT has some advantages compared with that supported by ImageJ. When the user interrupts the contour drawing using DerMAT, the contour remains open, but there is the possibility of resuming drawing until the user completes and closes the contour. In ImageJ when drawing is interrupted,

Table 3.1: Functional evaluation of DerMAT.

Criterion #	DerMAT	ImageJ	Labelme	Annotor
1	Freehand	Freehand and polygonal	Polygonal	Polygonal
2	Yes	Yes	Yes	Yes
3	Point-by-point and local reshaping	Point-by-point reshaping[a]	Point-by-point reshaping	Point-by-point reshaping
4	Binary mask	".roi" file format and binary mask	XML file format	XML file format

[a] The point-by-point reshaping mode available in ImageJ only works for polygonal segmentations.

the contour is automatically closed with a straight line between the beginning and the end point, and hence, if this line is not accurate enough, it is necessary to redraw the contour from the beginning. This issue is very important specially when the manual segmentation is performed using a pen tablet, since dermatologists often lift the pen from the tablet during the contour drawing (either to evaluate the correctness of the current segmentation status or simply to rest their hands).

The four tools under analysis allow segmenting and labeling multiple ROIs in an image, and hence all of them satisfy the second criterion.

The developed tool has better boundary reshaping functionalities than the other three tools under analysis. First of all, only DerMAT allows reshaping a contour performed by a freehand segmentation. Using the other three applications only polygonal segmentations can be reshaped. In addition, DerMAT has two different methods for boundary reshaping, namely pointwise and local boundary reshaping (see subsection 3.1.4), whereas the other tools only support the point-by-point boundary edition. The local boundary reshaping available in DerMAT can be very useful, since it provides a faster way to make great adjustments in the initial contour than the point-by-point reshaping method.

All the tools under evaluation are capable to save the manual segmentations and generate output data to be used as input in computer vision algorithms. By using our developed tool, DerMAT, each segmented region is stored as a binary image and associated to the respective label. This binary mask can be easily used to extract the boundary coordinates of every segmented region. Labelme and Annotor can produce a XML file containing information about the boundary positions and labels of each segmented object. In case of ImageJ, the segmented ROIs are stored as an ".roi" file. There is also the possibility to create and save a binary mask of each segmented region.

Besides these four fundamental criteria, DerMAT can offer other interesting functionalities such as: *a posteriori* boundary edition, and multi-user ground truth annotation and segmentation comparison (both described in subsections 3.1.5 and 3.1.6, respectively).

Summarizing, taking the four criteria into account DerMAT has some advantages with respect to other three existing annotation tools, namely better freehand drawing and boundary reshaping functionalities.

Chapter 4

Dermoscopic image segmentation

Image segmentation is one of the most important tasks in image processing, since its accuracy determines the eventual success or failure of computerized analysis procedures. The main purpose of the segmentation process is the partition of a given image into disjoint regions that are homogeneous with respect to one or more characteristics or features [53, 54].

In this work, segmentation is used in order to automatically extract the pigmented skin lesion from the surrounding skin in dermoscopic images. Before segmentation itself, a pre-processing procedure is applied to dermoscopic images with the principal aim of artifact removal and image smoothing.

In this chapter the pre-processing steps used in this work are first presented, followed by the description of all segmentation methods that were implemented. Then some experimental results are obtained in order to evaluate the performance of the segmentation methods.

4.1   Pre-processing

The pre-processing procedure used in this work can be divided into three main steps: (i) conversion of the image from the RGB (red-green-blue) color space to grayscale; (ii) image filtering; and (iii) detection of the dark regions in the four corners of the image. These three pre-processing steps are described in detail in the next subsections.

4.1.1   Conversion of the image from RGB to grayscale

The dermoscopic images used in this work are 8-bit RGB color images. Due to the computational simplicity of single channel (scalar) processing, the first step of the pre-processing is the conversion of the image from the RGB color space into a grayscale image. Therefore, three of the most common methods for grayscale conversion of dermoscopic images were considered and tested [9, 10], namely:

| (a) Original image | (b) Blue channel | (c) Luminance transformation | (d) Highest entropy channel ($\Rightarrow$blue) |

| (e) Original image | (f) Blue channel | (g) Luminance transformation | (h) Highest entropy channel ($\Rightarrow$red) |
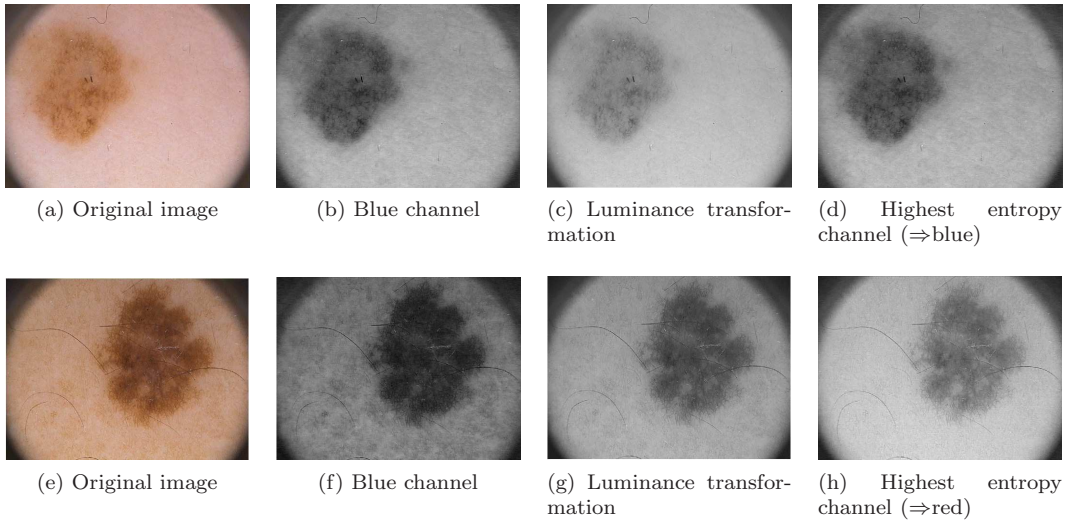
Figure 4.1: Conversion of the image from the RGB color space to grayscale.

1. **The selection of the blue color plane from the RGB color space:** it was experimentally established that the blue color plane is the one that provides the best discrimination between the lesion and the surrounding skin in most dermoscopic images.

2. **The application of the luminance transformation:** where the red (R), green (G), and blue (B) channels are linearly combined into a single channel (L) using the following equation:

$$L = 0.2989 \cdot R + 0.5870 \cdot G + 0.1140 \cdot B \tag{4.1}$$

3. **The selection of the RGB color component with the highest entropy:** entropy provides a measure of an image's smoothness in terms of gray level values. The higher the entropy, the more gray levels are present in the image [34]. In this approach, the entropy of each color component i is first computed:

$$S(i) = -\sum_{g=0}^{L-1} P(g) \cdot log_2[P(g)] \tag{4.2}$$

where $P(g)$ is the histogram of the color component i, and $L = 256$ corresponding to the number of gray levels. Then, the RGB color component with the highest entropy is selected:

$$i^* = \arg\max_i S(i) \tag{4.3}$$

After testing the three approaches for grayscale conversion in our dermoscopic image dataset, the blue color component was chosen for use since it demonstrated to be the RGB color channel where there is the best discrimination between the lesion and the skin (Figure 4.1). Moreover, among the tested approaches it is the one that provides the best performance for the segmentation methods.

4.1.2 Image filtering

In this work, the aim of filtering is image smoothing and also the elimination of some image artifacts, such as skin texture, air bubbles, and specially the features from dark hairs whose presence can reduce the accuracy of the segmentation methods. To accomplish this purpose, dermoscopic images are filtered with a hair removal filter followed by a median filter (both described in subsections 4.1.2.1 and 4.1.2.2, respectively).

4.1.2.1 Hair removal

Dermoscopic images sometimes contain some intrinsic skin features such as hairs, skin lines, and blood vessels. The presence of hairs in an image may occlude the skin lesion which leads the segmentation algorithms to fail. Therefore, the hair removal prior to segmentation is required.

There is a wide diversity of hair removal methods proposed in the literature [55]. Two different methods for hair removal were considered and tested: morphological close filtering, and a hair detection approach based on directional filters proposed in [56]. In a grayscale level, morphological closing removes dark details from an image and hence can be used for hair removal in dermoscopic images. However, as it is applied to the whole image there is a trade-off between hair removal and edge blurring, depending on the size of the structuring element. Besides hair removal, the second method provides a better edge preservation than morphological close filtering, since it is locally applied in the hair pixels. As result, the hair removal method used in this work is based on the methodology proposed in [56], due to its hair removal capability and better edge preservation.

The hair removal method can be divided into three main steps: (i) hair enhancement; (ii) hair segmentation; and (iii) hair disocclusion.

(i) Hair enhancement

Hairs appear as long and thin segments in dermoscopic images, that are usually darker than the skin. Therefore, the image is processed with a set of line detection filters in order to enhance hairs. As dermoscopic hairs may occur in any direction, it is necessary to apply a set of directional filters that can cover the entire range of possible orientations, $\phi_i \in [0, \pi[$, $i = 1, ..., N$. The line detection procedure is based on a difference of gaussians (DoG), which is defined as the difference between two Gaussians filters, $G_1(x, y)$ and $G_2(x, y)$, with the same mean and distinct variance:

$$g(x, y) = G_1(x, y) - G_2(x, y)$$
$$= k_1 e^{[-(\frac{x^2}{2\sigma_{x_1}^2} + \frac{y^2}{2\sigma_{y_1}^2})]} - k_2 e^{[-(\frac{x^2}{2\sigma_{x_2}^2} + \frac{y^2}{2\sigma_{y_2}^2})]}$$

$$(4.4)$$

where k_1 and k_2 are normalization constants. The rotation of $g(x, y)$ with angle ϕ is then implemented by using $g_{\phi_i}(x', y') = g(x, y)$, where $x' = x \cos \phi + y \sin \phi$ and $y' = y \cos \phi - x \sin \phi$. The variances of the Gaussians filters, $\sigma_{x_1}^2, \sigma_{y_1}^2, \sigma_{x_2}^2$, and $\sigma_{y_2}^2$ were defined so that the filter impulse response have a linear and highly directional shape.

Therefore, the response of each filter $g_{\phi_i}(x, y)$ to an input image $I(x, y)$ can be expressed as:

$$R_i(x, y) = g_{\phi_i}(x, y) \otimes I(x, y) \tag{4.5}$$

where $\otimes$ denotes the spatial convolution between $g_{\phi_i}(x, y)$ and $I(x, y)$. For each pixel, the highest filter response is kept in order to produce the final image output (Figure 4.2(b)).

(a) (b)

(c) (d)
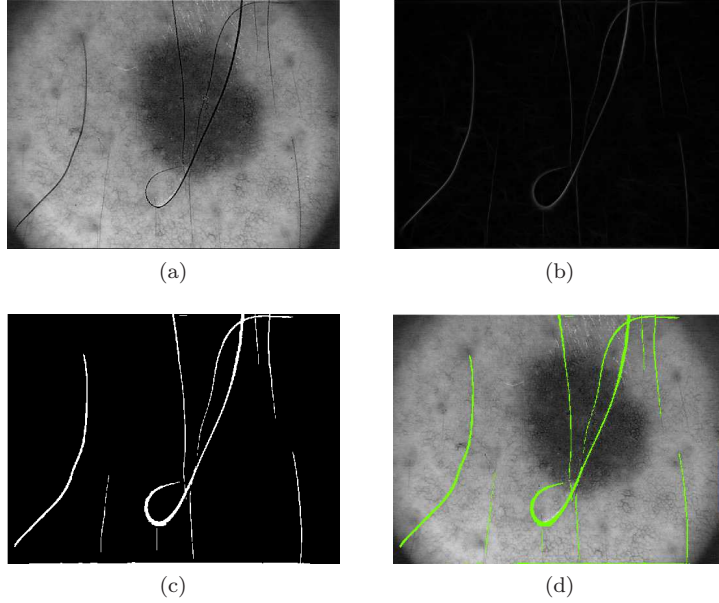
Figure 4.2: Hair detection: (a) Original grayscale image; (b) DoG filters response; (c) Binary hair mask; and (d) Hair mask superimposed on the original grayscale image.

(ii) Hair segmentation

The purpose of this step is to create a binary mask of the hairs (Figure 4.2(c)). Therefore, a global threshold T_{hairs} is applied to the filters response image $O(x, y)$:

$$B(x, y) = \begin{cases} 1, & \text{if } O(x, y) > T_{hairs} \\ 0, & \text{if } O(x, y) \leq T_{hairs} \end{cases} \tag{4.6}$$

where $B(x, y)$ is the binary hair mask, in which pixels with intensity value of 1 correspond to hairs, while pixels with value 0 correspond to the background. T_{hairs} was empirically defined based on the dermoscopic image dataset used in this work.

(iii) Hair disocclusion

Hair disocclusion is the process of restoring all the pixels that are originally occluded by hair. Therefore, a PDE-based inpainting algorithm is used to repaint the hair pixels based on the information gathered from surrounding areas (non-hair pixels).

In general, this inpainting technique fills in the area to be inpainted, Ω, by propagating information from its boundary, $\partial\Omega$, along level lines (called isophotes). The different regions inside Ω, as defined by the contour lines, are filled with color, matching those of $\partial\Omega$. The algorithm works iteratively, in which the region Ω is progressively shrunk in a smooth way [57].

Figure 4.3 shows the final output of the hair removal method. The original grayscale image image is shown in Figure 4.3(a), and the recovered image after using the inpainting algorithm can be shown in Figure 4.3(b).

(a)   (b)
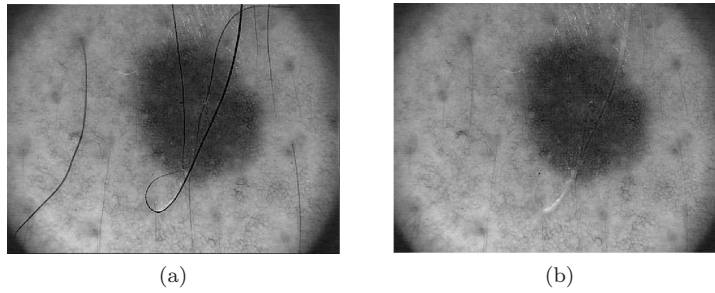
Figure 4.3: Hair disocclusion: (a) Original grayscale image; (b) Hair removal after image inpainting.

4.1.2.2 Image smoothing

After the hair removal step, dermoscopic images are filtered with a median filter in order to smooth the image as well as to remove some spurious points (or small dark dots). These spurious points may arise when the dark hairs are not completely eliminated in the hair removal step.

The median filter is a non-linear smoothing method that replaces the original gray level of a pixel by the median of the gray levels of the pixels in a specified neighborhood:

$$y(i,j) = median\left\{x(m,n), (m,n) \in w(i,j)\right\} \qquad (4.7)$$

where y is the input image, x is the output image, and w represents the neighborhood centered at image coordinates (i,j) [34, 58].

These filters are useful because of their noise-reduction capability, with considerably less blurring than linear smoothing filters of similar size. In addition, median filters are particularly effective in the elimination of impulse noise, in our case the dark spurious points, because the median of the gray levels in the neighborhood is not affected by individual noise spikes. This kind of noise cannot be otherwise eliminated by linear smoothing filters [34, 59, 60].

4.1.3 Detection of the dark regions in the four corners of the image

As result of using the dermatoscope to capture the skin lesion images, most of the images used in this work present four dark regions in their corners. In a grayscale level these regions have similar intensities to the lesion intensity, which can reduce the performance of some segmentation methods. Therefore, a binary mask of the dark corners is created to eliminate their influence on the segmentation results. To accomplish this purpose, Otsu's method is first applied to the image, and then the binary components that are connected with the four corners of the image are selected (Figure 4.4). Otsu's method is described in detail in the subsection 4.2.1.1.

The binary mask of the dark corners is used in most of segmentation methods that were implemented in this work. For instance, in histogram-based thresholding techniques, the pixels of the dark corners are not used in the computation of the image histogram. Furthermore, this binary mask is used to determine if the image has or not the dark regions in the four corners. This information is essential in the clustering segmentation methods, in which the number of clusters have to be defined as an input parameter of the algorithm.

(a)   (b)
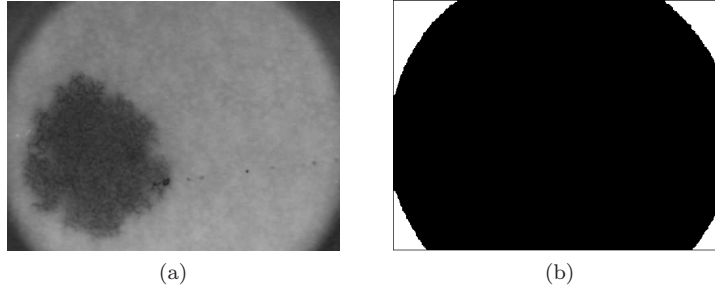
Figure 4.4: Corner mask creation: (a) Original grayscale image; (b) Binary mask of the dark regions in the four corners of the image.

4.2 Segmentation methods

Image segmentation is a process of partitioning an image into a set of disjoint regions that are homogeneous with respect to certain attributes (i.e. intensity, rate of change in intensity, color, or texture). The union of all regions must correspond to the whole image [59].

Image segmentation methods can be roughly divided into two main groups, namely feature domain and image domain methods. Feature domain methods are based on finding compact clusters in some feature space. Basically, several features (intensity, color, texture, etc) are measured at each pixel or region, and then organized into a feature vector. Then clustering or thresholding methods are used to segment the data. Image domain methods consider the spatial information of the image, and hence try to satisfy both feature-space homogeneity and spatial compactness simultaneously. Essentially, in these methods the connection among image pixels is considered in order to assign them to regions. These algorithms can be further classified into region-based
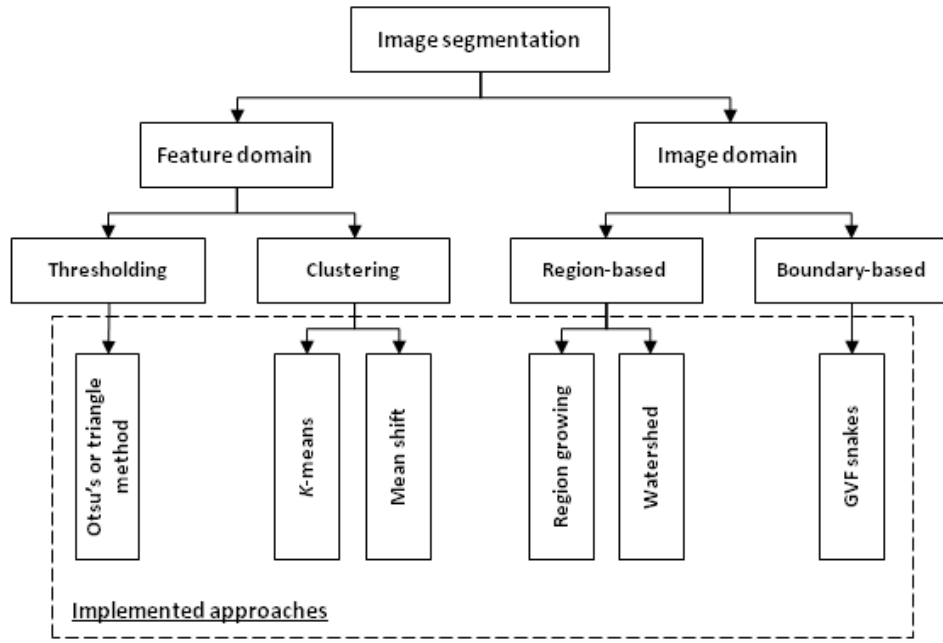
Figure 4.5: Classification of image segmentation methods (Adapted from [61]).

and boundary-based methods [61]. An overall classification of the image segmentation methods is illustrated in Figure 4.5.

Since there is a wide variety of image segmentation methods described in the literature, our efforts were focused into the most widely used algorithms. Therefore, several segmentation methods were implemented and tested, including: automatic thresholding, region growing, watershed, k-means, mean-shift, and gradient vector flow (GVF) snakes.

4.2.1 Automatic thresholding

Thresholding is a common image segmentation technique that is particularly useful for images containing solid objects resting on a contrasting background. In this technique, typically, a single threshold value is used to create a binary partition of the image intensities. Therefore, the image is divided into a group of pixels having values less than the threshold and a group of pixels with values greater or equal to the threshold. In general, a gray-level thresholding operation can be described as:

$$G(x, y) = \begin{cases} 1, & \text{if } I(x, y) \geq T \\ 0, & \text{if } I(x, y) < T \end{cases} \qquad (4.8)$$

where $I(x, y)$ is the original image, T is the threshold value, and $G(x, y)$ is the thresholded image. The result of thresholding is a binary image, where pixels with intensity value of 1 (or any other convenient gray level) correspond to objects, while pixels with value 0 (or any other gray level not assigned to objects) correspond to the background [34, 54].

Thresholding has the advantages of being computationally simple and fast, and produces good

35

results on images that contain objects with uniform intensity values on a contrasting background. One of the major drawbacks of this technique is that the segmentation result significantly depends on the threshold used. Even a small change in the threshold value can produce a different segmented region. Moreover, as thresholding does not consider the spatial information of an image, it is very sensitive to noise and intensity inhomogeneities [30, 62].

The thresholds are usually generated interactively by using visual feedback. Several algorithms have been proposed in order to automate the process of finding correct thresholds [62]. A survey on automatic thresholding techniques is provided in [63].

The histogram of the dermoscopic images can essentially be either bimodal or unimodal. According to each situation different algorithms are employed for automatic thresholding. If the image histogram has two major peaks (bimodal image) then the threshold value is obtained through Otsu's method, while if the image histogram has a single peak (unimodal image) the threshold value is obtained by the triangle method. The implementation details are described in subsection 4.2.1.3.

These two automatic thresholding techniques were chosen because Otsu's method is one of the most popular techniques that produces good results in bimodal images, and because the triangle algorithm is known to be particularly effective when the image histogram has a single large peak and a long tail [34]. In the following subsections, Otsu's and Triangle methods are described in more detail.

4.2.1.1 Otsu's method

Otsu's algorithm [28] is one of the most popular techniques of optimal thresholding that produces good results in bimodal images. This method maximizes the likelihood that the threshold is chosen so as to split the image between an object and its background. This is achieved by selecting a threshold that gives the best separation of classes, such that the between-class variance is maximized and the intra-class variance is minimized [64].

This technique is based on a discriminant analysis which divides the image into two classes C_0 and C_1 by threshold k, such that $C_0 = \{0, 1, 2, ..., k\}$ and $C_1 = \{k+1, k+2, ..., L-1\}$, where L is the total number of the gray levels of the image (Figure 4.6).

The grey-level histogram is normalized and considered as a probability distribution. The probability of occurrence of level i is given by $p_i = n_i/N$, where n_i denotes the number of pixels at the ith gray level and N denotes the total number of pixels in a given image [65, 66].

This can be used to compute then zero- and first-order cumulative moments of the normalized histogram up to the kth level as: $\omega_0(k) = \sum_{i=1}^{k} p(i)$, $\mu_0(k) = \sum_{i=1}^{k} i \cdot p(i)/\omega_0$. The total mean level of the image is given by: $\mu_T = \sum_{i=1}^{L} i \cdot p(i)$ [64, 65].
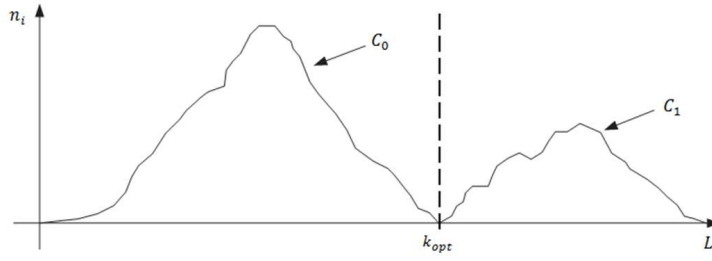
Figure 4.6: Optimal thresholding, k_{opt}, achieved by Otsu's algorithm (Adapted from [64]).

Otsu's algorithm looks for the intensity threshold k that maximizes one of the following criterion measures (or measures of class separability):

$$\eta = \sigma_B^2/\sigma_T^2 \text{ or } \lambda = \sigma_B^2/\sigma_W^2 \text{ or } \kappa = \sigma_T^2/\sigma_W^2 \tag{4.9}$$

where σ_T^2, σ_B^2, and σ_W^2 represent the total variance of the image, the between-class variance, and the within-class variance, respectively:

$$\sigma_W^2 = \omega_0\sigma_0^2 + \omega_1\sigma_1^2 \tag{4.10}$$

$$\sigma_B^2 = \omega_0\omega_1(\mu_1 - \mu_0)^2 \tag{4.11}$$

$$\sigma_T^2 = \sigma_W^2 + \sigma_B^2 \tag{4.12}$$

where $\omega_1 = 1 - \omega_0$, and $\mu_1 = \sum_{i=k+1}^{L} i \cdot p(i)/\omega_1$. The measure η is the simplest one to maximize, because σ_T^2 does not depend on k. The optimal threshold k_{opt} that maximizes η, or equivalently maximizes σ_B^2 is given by [28, 65, 67]:

$$
\begin{aligned}
k_{opt} &= \arg\max\left\{\eta(k)\right\} \\
&= \arg\max\left\{\sigma_B^2(k)\right\}
\end{aligned}
\tag{4.13}
$$

4.2.1.2 Triangle method

The triangle algorithm [68] is known to be particularly effective when the object pixels produce a weak peak in the histogram. This technique is illustrated in Figure 4.7, where low gray-level objects reside on a high gray-level background.

This algorithm starts by finding the maximum peak of the histogram. This is followed by determining the line passing through the maximum peak point $[I_{max}, H(I_{max})]$ and the lowest point $[I_{lowest}, H(I_{lowest})]$ in the histogram. The distance, D, from this line to the histogram is computed for each intensity $H(I)$, with I ranging from I_{lowest} to I_{max}. The optimal threshold, T, is selected as the intensity that maximizes the distance D [34, 67].
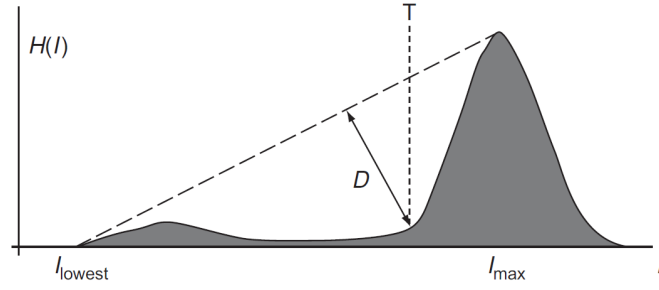
Figure 4.7: Illustration of the triangle algorithm. The triangle algorithm selects the intensity threshold (T) that maximizes the distance, D, between the line and the histogram (Adapted from [34]).

4.2.1.3 Implementation

After analyzing the histogram of dermoscopic images it was verified that most of the images have a bimodal histogram, in which one of these modes corresponds to the lesion and the other to the skin (Figures 4.8(a) and 4.8(b)). However, there are a few exceptions. Some images have a unimodal histogram, either when the lesion is very small compared to the skin, or when the lesion is very large and covers almost the entire image. In these cases the lesion pixels produce a weak peak in histogram, as shown in Figures 4.8(c) and 4.8(d).
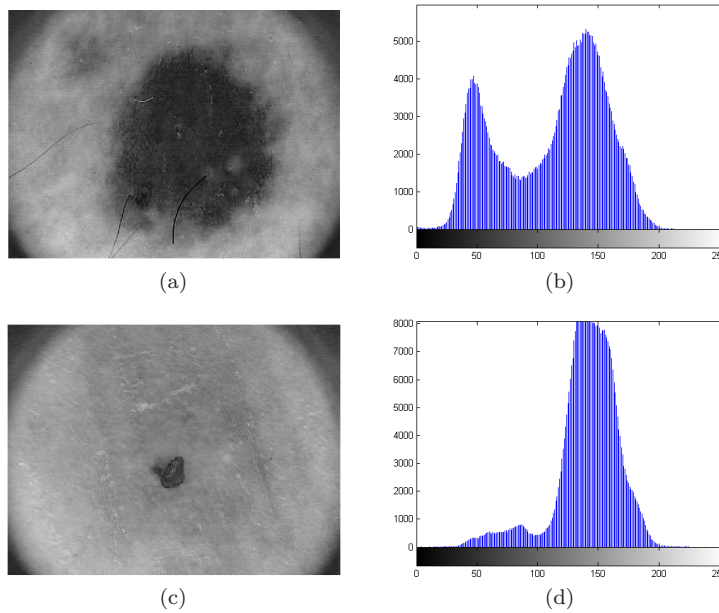
Figure 4.8: Examples of histograms of dermoscopic images: (a) Dermoscopic image; (b) Histogram of (a); (c) Another example of dermoscopic image; and (d) Histogram of (c).

Therefore, an algorithm for automatic detection of the number of significant histogram peaks (local maxima) was developed. Based on this algorithm an appropriate automatic thresholding method is used to segment the images. If the image histogram has two major peaks then the threshold is obtained through Otsu's method, else if the image histogram has a single peak the threshold value is obtained by triangle method.

Algorithm for significant histogram peaks detection

The main objective of this algorithm is to automatically define which of the thresholding techniques will be used in each image. For this purpose, the local maxima of the image histogram are computed in order to evaluate if the image histogram is bimodal or unimodal. The steps of the algorithm are as follows:

Histogram smoothing: a median filter is used to remove noise and smooth the image histogram. Besides the histogram smoothing, this filter also eliminates some outliers that could make the determination of local maxima more difficult.

Determination of local maxima: an intensity level is considered a local maximum if the corresponding number of pixels is greater or equal than the average of number of pixels of the intensity levels in a predefined neighborhood (in this case a 1×13 neighborhood is used).

In this phase a large number of local maxima are computed. In order to keep at most two significant ones (one corresponding to the lesion and another to the skin), these local maxima must satisfy the following three conditions.

1. The local maxima must have a corresponding number of pixels greater than a certain threshold T_1. This value was empirically defined as 150, because the modes corresponding to the lesion and to the skin have always a number of pixels greater than T_1.

2. The intensity difference between two consecutive local maxima must be greater than a threshold T_2. The purpose of this parameter is to ignore smaller peaks that may occur in close proximity to a large local peak. The threshold value was empirically defined based on the image dataset as $T_2 = 35$.

3. In case there are more than one local maximum, the one with lowest intensity must have an intensity value lower than a threshold T_3. This threshold is used to ensure that at least one of the local maxima corresponds to the lesion, because usually the lesions have low intensities. The threshold value was also empirically defined as $T_3 = 140$.

After this procedure, the algorithm defines which of the thresholding methods is used, based on the number of detected local maxima. Therefore, if the image histogram has a single maximum the triangle method is applied. When the image histogram has two dominant maxima then the threshold is obtained through Otsu's method. However, if one of these maxima is a weak peak the triangle method is also used. A weak peak is a local maximum with a number of pixels lower than 900 (empirically defined value). For example, as shown in Figure 4.9, where two dominant peaks are detected, the Otsu's method is used for segmentation.
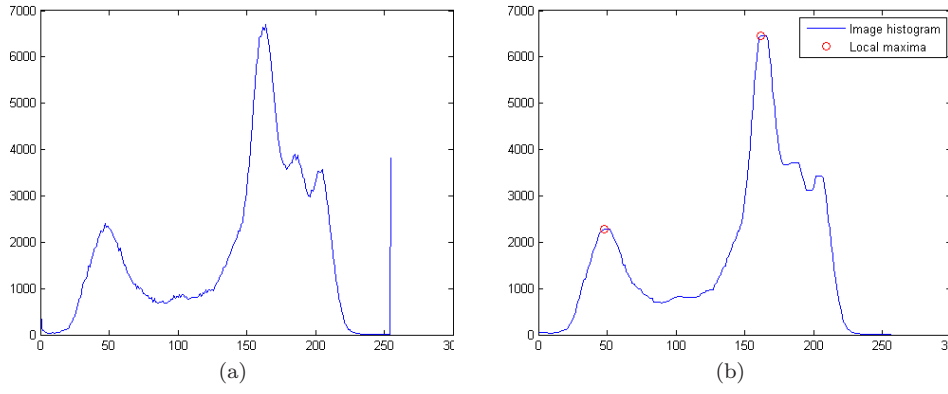
Figure 4.9: Algorithm for significant histogram peaks detection: (a) Original image histogram; (b) Histogram peaks detection (note that two local maxima/peaks are detected, and this histogram is smoother than (a) and without the outlier).

4.2.2 k-means

The k-means algorithm is an unsupervised clustering algorithm that classifies the input data points into multiple classes based on their inherent distance from each other. Thus, a set of data points are grouped into k disjoint subsets (clusters) S_i, $i = 1, 2, ..., k$, each one represented by a centroid, so as to minimize the sum-of-squared error function:

$$V = \sum_{i=1}^{k} \sum_{x_n \in S_i} |x_n - \mu_i|^2 \tag{4.14}$$

where x_n is the value of the nth data point, and μ_i is the geometric centroid of the data points within the cluster S_i.

The algorithm proceeds by iterating two steps. In the first step each data point (feature) is assigned to its closest centroid. In the second step each centroid μ_i is updated by computing the mean of the features that were assigned to cluster i. This iterative process drives the objective function towards a minimum. The resultant grouping of the data points is geometrically as compact as possible around the centroids in each cluster [69, 70]. The k-means algorithm can be summarized as follows:

1. Choose k initial centroids.

2. Assign each pixel in the image to its closest cluster by calculating distances among the pixel and all cluster centroids.

3. Re-compute the value of each centroid by averaging all of the pixels in the cluster.

4. Repeat steps 2 and 3 until the values of the centroids do not change [70, 71].

4.2.2.1 Implementation

The implementation of the k-means algorithm for image segmentation requires, essentially, the definition of four input parameters, including the input data, the number of classes, the initial

cluster centroid positions, and a distance measure.

Most of the dermoscopic images of our dataset have three distinct regions, such as the lesion, the skin, and also the dark regions in the four corners of the image. However, some images have not the dark regions in the four corners, so in these cases the dermoscopic images are composed only by two distinct objects, including the lesion and the surrounding skin. Therefore, the number of classes used in the k-means algorithm can be either three, or two depending on the presence or not of the regions in the four corners, respectively. The definition of the number of classes is automatically done based on the corner mask that is obtained in the pre-processing step (see section 4.1.3).

In an initial phase, the initial cluster centroid positions were randomly assigned. However, it was observed that, in this way, the algorithm could have a poor performance, specially in the images where there is a low contrast between the lesion and the surrounding skin. In order to overcome this drawback, the initial cluster centroid positions are defined based on the corner mask as well as on the initial snake curve that is used in the automatic initialization of the GVF snake method. The determination of this curve is further described in detail in section 4.2.5.1. The initial snake curve and the corner mask are used to create a binary mask of each cluster (lesion, skin, and dark regions in the four corners) and the initial cluster centroid positions are defined as the mean intensity of these masks.

In this method, the blue color component from the RGB color space is used as the input data. Other characteristics, such as the spatial information of the image (position vectors in x and y), and the image gradient, were combined with the image intensity in an attempt to improve the segmentation performance. However, the best segmentation results were obtained using only the blue color component from the RGB color space.

(a)   (b)
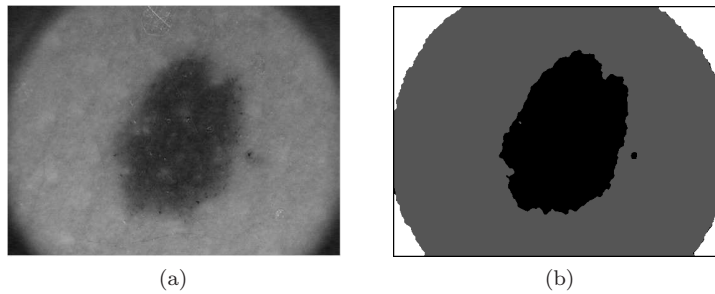
Figure 4.10: k-means clustering segmentation: (a) Original grayscale image; and (b) Result of k-means segmentation, for $k = 3$.

Figure 4.10 shows the result of k-means clustering segmentation. In this case the original image is partitioned into three classes, corresponding to the lesion (black region), to the skin (gray region), and to the regions in the four corners of the image (white region). After image clustering, a set of post-processing operations are applied to the class that contains the lesion in order to keep the largest binary object from the image, to join small adjacent regions, and to

smooth the contours. The post-processing step is described in subsection 4.3.

4.2.3 Mean shift

The mean shift algorithm is a non-parametric mode finding/clustering procedure. The concept underlying mean shift is to cluster an image by associating each pixel with a mode (local maximum) of the probability density of the image. The local maxima are identified in an iterative process using a density kernel estimator. The outcome of mean shift is only controlled by the kernel size (or bandwith) of the density kernel estimator. Therefore, this algorithm does not require prior knowledge of the number of clusters and does not constrain their shape [72, 73].

Given n data points x_i, $i = 1, ..., n$, in a d-dimensional space R^d, the multivariate kernel density estimator, obtained with kernel $K(x)$ and computed at point x, is given by:

$$f(x) = \frac{1}{nh^d} \sum_{i=1}^{n} K \left(\frac{x - x_i}{h} \right) \tag{4.15}$$

where h denotes the kernel size. For practical purposes, radially symmetric kernels $K(x)$ are commonly used satisfying:

$$K(x) = c_{k,d} k(\|x\|^2) \tag{4.16}$$

where $c_{k,d}$ is a normalization constant that makes $K(x)$ integrate to 1. The modes of the density function are located at the zeros of the gradient of the density estimator, $\nabla f(x) = 0$. The gradient of the density estimator, after some further algebraic manipulation, is given by:

$$\nabla f(x) = \frac{2c_{k,d}}{nh^{d+2}} \left[\sum_{i=1}^{n} g \left(\left\| \frac{x - x_i}{h} \right\|^2 \right) \right] \left[\frac{\sum_{i=1}^{n} x_i g \left(\left\| \frac{x - x_i}{h} \right\|^2 \right)}{\sum_{i=1}^{n} g \left(\left\| \frac{x - x_i}{h} \right\|^2 \right)} - x \right] \tag{4.17}$$

where $g(x) = -k'(x)$ denotes the kernel's profile derivative. The first term of Eq. 4.17 is proportional to the density estimator at x, computed with the kernel $G(x) = c_{g,d}(\|x\|^2)$. The second term of Eq. 4.17 represents the mean shift vector, $m_h(x)$, that provides the direction of the gradient of the density estimator at x, and always points towards the direction of the maximum increase in the density.

The mean shift procedure is obtained by successive computation of the mean shift vector and translation of the kernel $K(x)$ by $m_h(x)$. Hence, it converges along a path leading to a mode of the density. The set of all locations that converge to the same mode defines the basin of attraction associated with this mode. The points which are in the same basin of attraction are associated with the same cluster [60, 72, 73].
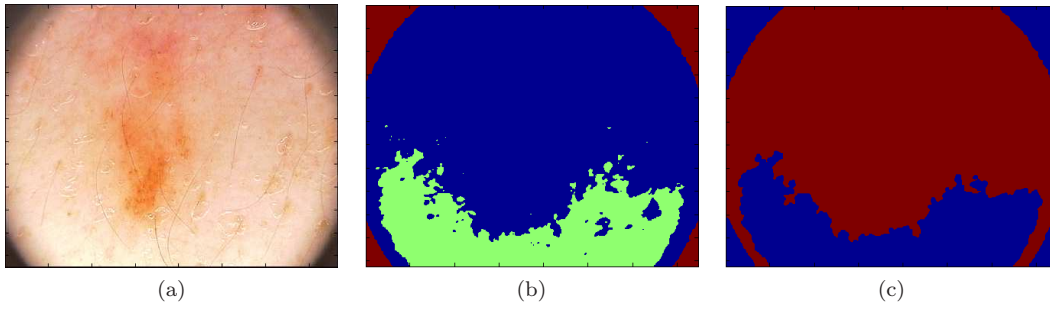
Figure 4.11: Mean shift clustering applied to obtain 3 clusters: (a) Original RGB image; (b) Result of mean shift clustering; and (c) Bad segmentation result.

4.2.3.1 Implementation

The only free parameter in the mean shift algorithm is the size of the density kernel estimator. As dermoscopy images can present two or three objects (depending on the absence or not of the dark corners), the initial idea consisted of iteratively varying the size of the kernel until two or three clusters are obtained. However, it was observed that in images with a very low contrast between the lesion and the surrounding skin the algorithm could produce bad results (Figure 4.11) or even not converge into two/three clusters, independently of the radius of the kernel.

To overcome this problem, the mean shift algorithm is applied to obtain at least five clusters. If less than five clusters are obtained, the radius of the used kernel is iteratively decreased and then the mean shift procedure is repeated. This number of clusters has proved to be sufficient to obtain good results after subsequent merging.

After clustering, the adjacent clusters are merged based on the mean intensity of each cluster. Given two adjacent clusters, C_i and C_j, the merging procedure is given by:

$$C_m = C_i \cup C_j, \qquad if \ \left| I_{C_i} - I_{C_j} \right| \leq T_m \qquad (4.18)$$

where C_m is the merged region, I_{C_i} and I_{C_j} are the mean intensities of C_i and C_j. Therefore, adjacent clusters are only merged if the difference between the mean intensity of the clusters is less than a threshold T_m. T_m was experimentally defined based on the dermoscopic image dataset used in this work.

Figure 4.12 shows two successful segmentation examples using the mean shift algorithm to obtain at least five clusters. The image in the first row (Figure 4.12(a)) was partitioned into thirteen clusters whereas the image in the second row (Figure 4.12(d)) was partitioned into six clusters. Then the merging procedure guarantees, in both cases, a successful final segmentation result.

By analyzing the figures 4.12 and 4.11, it is possible to observe that this procedure (applying the mean shift algorithm to obtain at least five clusters and then merge the adjacent clusters) provides better segmentation results than the results obtained when the mean shift algorithm is
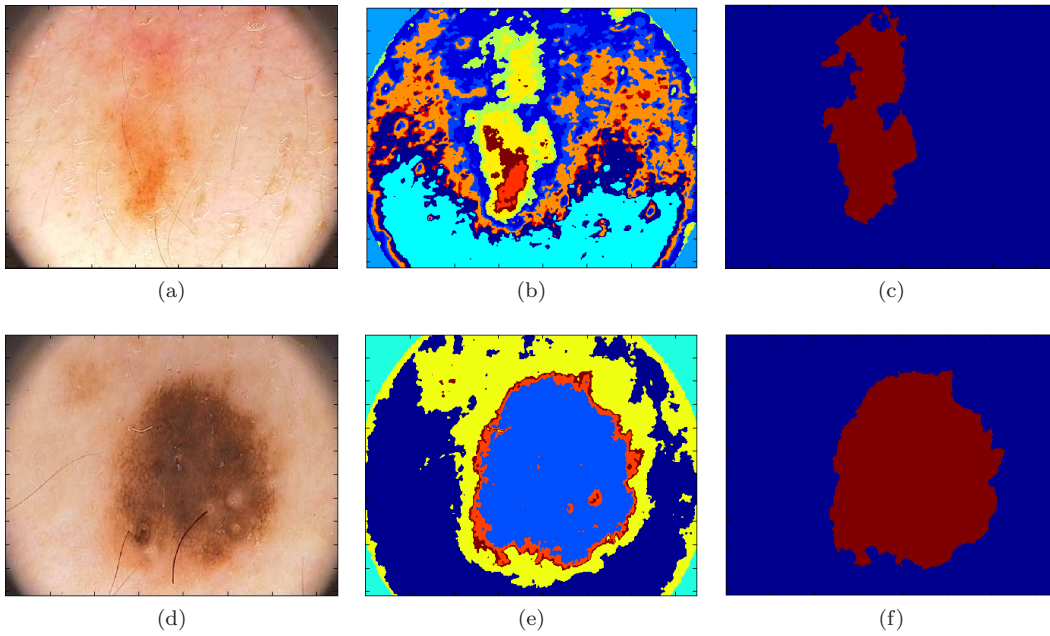
Figure 4.12: Mean shift clustering applied to obtain at least 5 clusters: (First column) Original RGB images; (Second column) Result of mean shift clustering; (Third column) Final segmentation result after merging procedure.

applied to obtain only three clusters.

4.2.4 Region growing

Region growing is a region-based segmentation method that exploits spatial context by grouping adjacent pixels or subregions into larger regions based on homogeneity criteria. The parameters that distinguish different objects may include average gray level, texture, color, etc [34, 53].

This technique starts with a pixel or a group of pixels, known as the seeds, which belong to the object of interest. These seeds can be either manually defined by the user or provided by an automatic seed finding procedure. In the next step, the neighboring pixels are examined one at a time and added to the growing region, if those pixels have properties similar to the seed (based on a homogeneity criterion). This process is applied iteratively until no more pixels satisfy the homogeneity criterion for inclusion in the growing region. The segmented object is then represented by all pixels that have been merged during the growing procedure [53, 54].

Region growing has the advantage of correctly segmenting regions that have the same properties and are spatially separated. Moreover, it generates connected regions. One of the main issues in region growing is the selection of a homogeneity criterion. When the homogeneity criterion is not properly chosen, the regions may leak out into adjoining areas or merge with regions that do not belong to the object of interest [54].

44
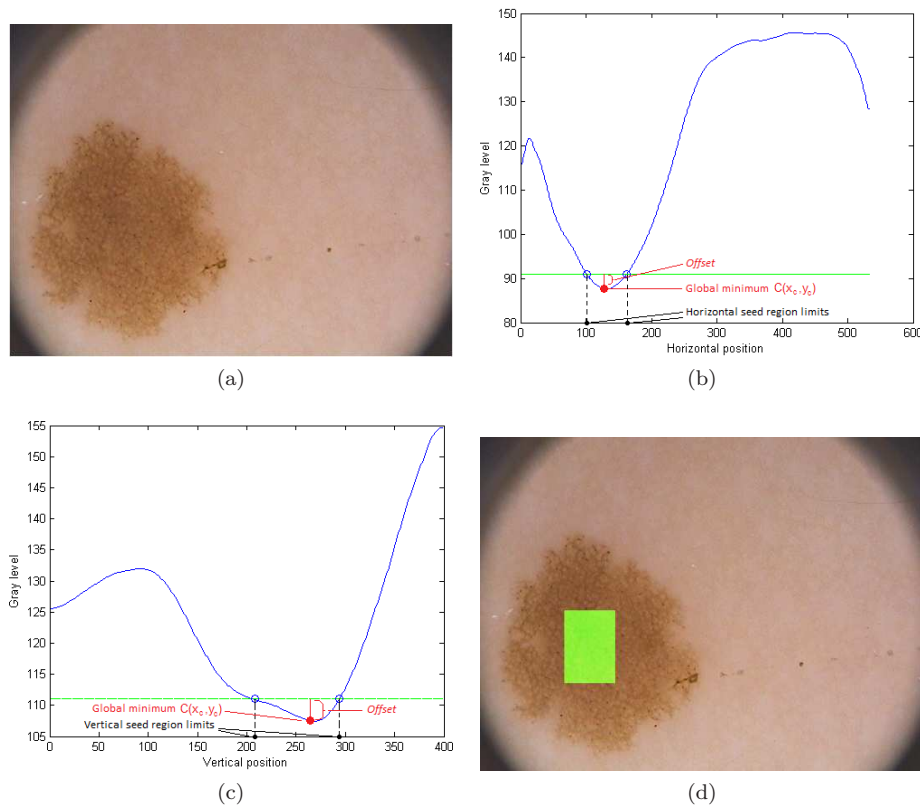
Figure 4.13: Automatic seed finding procedure: (a) Original RGB image; (b) Vertical projection P_y; (c) Horizontal projection P_x; and (d) Seed region (marked as a green rectangle) superimposed on the original image.

4.2.4.1 Implementation

The application of the region growing algorithm for dermoscopic image segmentation requires the definition of the initial seed position, the homogeneity criterion, and the stopping criterion.

- **Initial seed definition:** an algorithm for automatic seed finding was implemented in order to make the region growing method fully automatic. Therefore no kind of user intervention is required in the initialization procedure. This algorithm is further described at the end of this section.

- **Homogeneity criterion:** the difference between the intensity of a neighboring pixel and the mean intensity value of the growing region is used as homogeneity criterion. If the difference is less than a predefined threshold, the pixel is allocated to the growing region. Otherwise, it is defined as a background pixel.

- **Stopping criterion:** the growing process stops when no more neighboring pixels satisfy the homogeneity criterion.

45
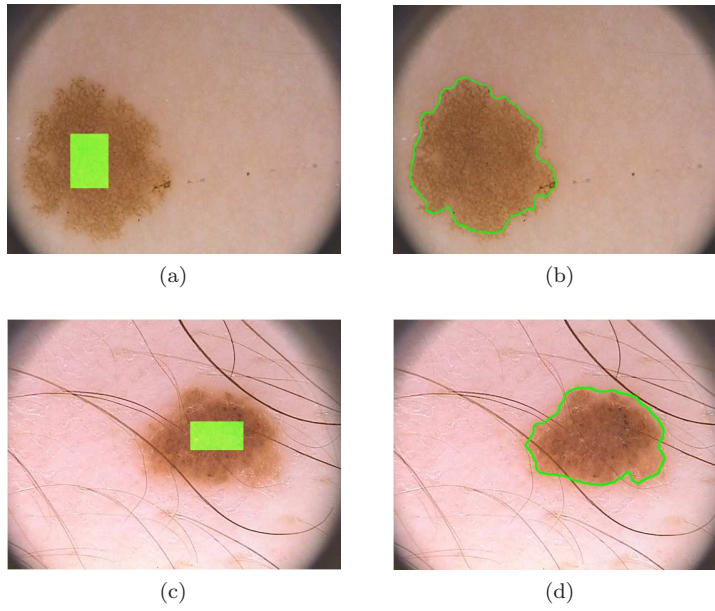
Figure 4.14: Segmentation examples obtained using region growing: (First column) Seed regions superimposed on the original images; (Second column) Final segmentation results.

The automatic seed finding procedure is based on the vertical and horizontal projections of the image. The vertical projection of an image, $I(x, y)$, is a function of the horizontal index y:

$$P_y = \frac{\sum_{x=1}^{n} I(x, y)}{(n - C_y)} \tag{4.19}$$

where n is the total number of lines of $I(x, y)$, and x is the vertical index. C_y corresponds to the number of pixels, in column y, belonging to the dark regions in the four corners of the image. The normalization by $(n - C_y)$ is used to reduce the influence of the dark corners in the image projection. C_y is computed using the corner mask obtained in the pre-processing step (see subsection 4.1.3). A similar procedure is used to compute the horizontal projection P_x.

The next step consists in the determination of the global minima of both vertical and horizontal projections. Since skin lesions are darker than the surrounding skin, the global minimizers of the image projections are used to provide the coordinates of a pixel $C(x_c, y_c)$ within the lesion, such as: $P_{x_c} = min(P_x)$ and $P_{y_c} = min(P_y)$.

The pixel $C(x_c, y_c)$ could be used as seed in region growing. However, due to skin lesion variability, such as small dots or regions with high intensity difference with respect to the remainder lesion, a single pixel used as seed may not grow properly until the lesion boundaries if the seed location happens to match such regions.

Therefore, a seed region (group of pixels) is used instead of a single pixel. First, a predefined offset is added to the global minima of the image projections, and then an horizontal line passing through this point is defined. The two points of intersection between the horizontal line and the image projection are computed and used to define the limits of the seed region. The resulting

seed region has a rectangular shape centered at $C(x_c, y_c)$. The horizontal limits of the seed region are obtained by the vertical projection whereas the vertical limits are obtained by the horizontal projection. The automatic seed region procedure is illustrated in Figure 4.13.

Figure 4.14 shows two segmentation examples using the region growing algorithm as well as the seed regions superimposed on the original images.

4.2.5 GVF snakes

The gradient vector flow (GVF) snakes method is an extension of the traditional snakes or active contours method. For better understanding, the background of traditional snakes is first presented followed by the description of the GVF concept.

Snakes are deformable curves defined within an image domain that can move towards the desired features, typically edges, under the influence of internal and external forces computed from the curve itself and the image data, respectively [74].

The evolution of the snake from an initial position to the object boundaries is expressed as an energy minimization process. The snake is defined by a parametric curve $v(s) = (x(s), y(s))$, where x and y are the coordinates along the contour, and $s \in [0, 1]$ is the parametric domain. The energy functional to be minimized is a sum of internal and image forces, and can be written as:

$$E_{snake} = \int_0^1 E_{int}(v(s)) + E_{image}(v(s))ds \qquad (4.20)$$

where E_{int} denotes the internal energy that controls the arrangement of the snake points, and hence the way the contour can stretch and curve. E_{image} is the image energy that attracts the snake towards the boundaries of the target object [36, 64, 74].

The internal energy is modeled using two terms, namely the first- and second-order derivatives around the contour:

$$E_{int} = \alpha(s) \left| \frac{dv(s)}{ds} \right|^2 + \beta(s) \left| \frac{d^2v(s)}{ds^2} \right|^2 \qquad (4.21)$$

The first-order term of Eq. 4.21 corresponds to the elastic energy that measures the energy due to stretching. Thus, a high elastic energy value implies a high rate of change in that region of the contour. The second-order term of Eq. 4.21 is the curvature energy, which measures the energy due to bending. The weighting parameters, $\alpha(s)$ and $\beta(s)$, represent the relative influence of the corresponding energy terms. The parameter $\alpha(s)$ controls the contribution of the elastic energy due to point spacing, whereas $\beta(s)$ controls the contribution of the curvature energy due to point variation [64, 75].

The image energy, E_{image}, is derived from the image data so that it takes on its smaller values at the features of interest, such as edges. Typically, the image energy designed to lead a

snake toward image edges is given as:

$$E_{image} = -\left|\nabla I(x,y)\right|^2 \tag{4.22}$$

where $I(x,y)$ is a gray-level image, and ∇ is the gradient operator. Therefore the snake is attracted to the edges with large image gradients [74, 75].

There are two main limitations with traditional snake algorithms applied to boundary segmentation. First, the initial contour must be close to the true object boundaries because of the small capture range of the image gradient, and also because of the presence of image artifacts. The second weakness of these approaches is the difficulty with expanding into boundary concavities. To overcome both of these problems, the gradient vector flow (GVF) can be used, in the snake equation (4.20), as external energy rather than the image gradient [36, 74].

The GVF field is computed as a diffusion of the gradient vectors of a gray-level or binary edge map derived from the image. The GVF field $\mathbf{g}(x,y) = [u(x,y), v(x,y)]$ is defined as the equilibrium solution that minimizes the following energy functional:

$$\epsilon = \int\int \mu(u_x^2 + u_y^2 + v_x^2 + v_y^2) + \left|\nabla f\right|^2 \left|\mathbf{g} - \nabla f\right|^2 dxdy \tag{4.23}$$

where f is the edge map of a given image, and μ is a regularization parameter that controls the degree of smoothness of the GVF field, and hence should be defined according to the amount of noise present in the image. The edge map f should take high values at the edges; it can be taken, for instance, as $f(x,y) = -E_{image}$ [60, 74].

The first term within the integrand is referred to as the smoothing term since this term alone will produce a slowly varying vector field. This happens when $\left|\nabla f\right|$ is small, and hence the energy is dominated by sum of the squares of the partial derivatives of the vector field. On the other hand, when $\left|\nabla f\right|$ is large, the second term dominates the integrand. Therefore, the GVF field points towards the boundaries when in their proximity and varies smoothly over homogeneous regions all the way to image boundaries. Consequently, it provides a large capture range and the capability to segment object concavities [54, 60, 74].

4.2.5.1 Implementation

The application of the GVF snakes method for the segmentation of a skin lesion is illustrated in Figure 4.15. In this particular example the evolution of the snake from the initial position (Figure 4.15(a)) to the skin lesion boundaries is achieved after 70 iterations (Figure 4.15(b)).

An automatic snake initialization method was implemented in order to make the segmentation process fully automated. This method is mainly based on the information obtained from the Canny edge detector [76], and can be described into three main steps, namely (i) edge detection;

(ii) edge validation; and (iii) initial curve determination.

(a)   (b)
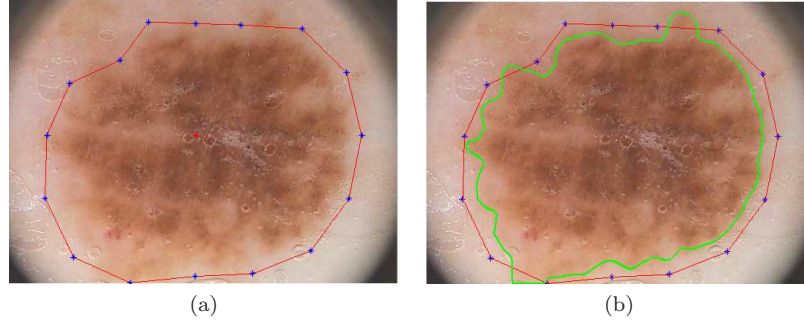
Figure 4.15: GVF snake segmentation: (a) Initial snake contour; (b) Final segmentation seg-
mentation result (green contour) after 70 iterations.

(i) Edge detection

The aim of this step is to create a binary edge map from the gray-level image. To accomplish
this purpose, the Canny edge detector algorithm is used.

The Canny operator is a multistage edge-detection algorithm. The input image $f(x, y)$ is
first smoothed using a Gaussian filter $G(x, y, \sigma)$ with a certain standard deviation σ, in order to
obtain:

$$f_s(x, y) = G(x, y, \sigma) \otimes f(x, y) \tag{4.24}$$

where $f_s(x, y)$ denotes the smoothed image. The Gaussian is defined as:

$$G(x, y, \sigma) = ke^{-(\frac{x^2+y^2}{2\sigma^2})} \tag{4.25}$$

where k is a normalization constant [34, 77].

Afterwards, a first-derivative operator (in this case the Sobel operator, [78], is used) is applied
to the smoothed image to calculate the magnitude and the direction of the gradient at each pixel.
Therefore, the gradient of the smoothed image $f_s(x, y)$ is obtained by convolving the image with
the pair of horizontal and vertical derivative kernels of the Sobel operator, g_x and g_y, yielding:

$$G_x = f_s(x, y) \otimes g_x, \quad G_y = f_s(x, y) \otimes g_y \tag{4.26}$$

where G_x and G_y denote the image gradients in the x and y directions, and the orthogonal
kernels, g_x and g_y, are given by:

$$g_x = \begin{bmatrix} -1 & 0 & 1 \\ -2 & 0 & 2 \\ -1 & 0 & 1 \end{bmatrix}, \quad g_y = \begin{bmatrix} -1 & -2 & -1 \\ 0 & 0 & 0 \\ 1 & 2 & 1 \end{bmatrix} \tag{4.27}$$

The magnitude of the gradient at each pixel $m(x, y)$ is given by:

$$m(x, y) = \sqrt{G_x^2 + G_y^2} \tag{4.28}$$

and the direction of the gradient $\theta(x, y)$ can be computed from the ratio of G_y and G_x by:

$$\theta(x, y) = \arctan\left(\frac{G_y}{G_x}\right) \tag{4.29}$$

The next step of the Canny edge detector is the non-maximum suppression process. This process thins the edges of the gradient magnitude image $m(x, y)$ by suppressing those pixels for which their gradient magnitude is not a local maximum along the direction of the gradient [34, 77].

After non-maximum suppression, the edge map is obtained using a dual-threshold mechanism, known as thresholding with hysteresis. This process uses two thresholds T_{low} and T_{high}. Then, all pixels with a gradient magnitude larger than T_{high} are considered as edge points. For pixels with values between T_{low} and T_{high}, a pixel is classified as an edge point only if it is adjacent to a pixel with a gradient magnitude greater than T_{high}. This recursive threshold, extends and fills in the edges determined by T_{high} [34, 77].

The binary edge map obtained through the Canny edge detector is visible in Figure 4.16(b), in which each pixel is labeled as either an edge point (value 1) or a nonedge point (value 0).

(ii) Edge validation

At this stage the edge map includes a large number of false positives edge segments. These false positives are usually resulting from the presence of the dark regions in the four corners of the image, and also from pigment network segments, skin lines, and even hairs when these artifacts have not been completely removed in the pre-processing step. Therefore, the edge segments corresponding to the dark corners are first eliminated, making use of the corner mask created in the pre-processing step (see subsection 4.1). Then, since edges of the skin lesions are larger than most of noisy edges, the length is used as a criterion in order to eliminate the edges whose length is less than a predefined threshold. The effect of this step is illustrated in Figure 4.16(c).

The next step aims to quantify the relative importance of each edge. To accomplish this purpose, the peripheral regions of each edge are identified (Figure 4.16(d)). These two regions in both sides of the edges are obtained with the application of a morphological dilation to each edge individually. It is important to note that the pixels immediately adjacent to the edges are not considered in the peripheral regions in order to reduce the relative importance of the edges created by small transitions (i.e. skin lines, hairs, etc).

The difference between the mean intensity of the peripheral regions is computed as a measure
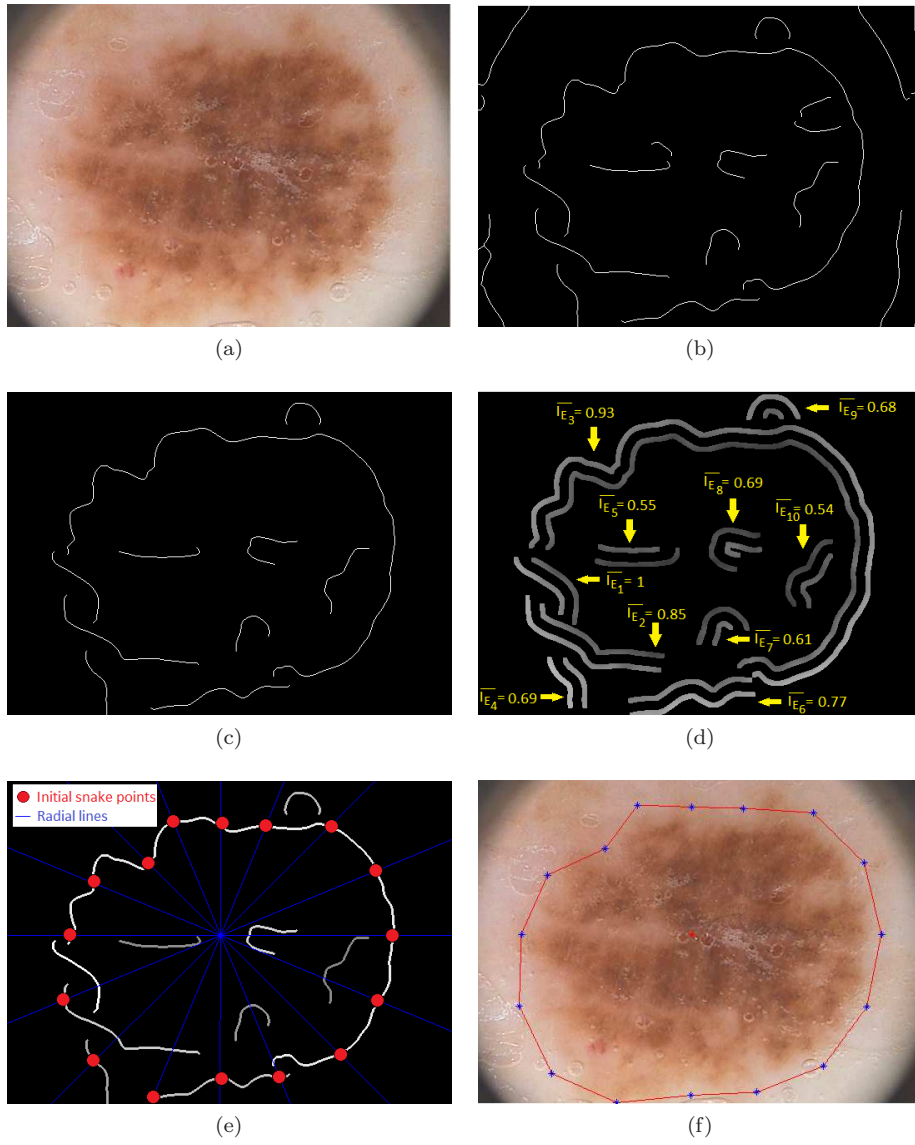
Figure 4.16: Automatic snake initialization method: (a) Original RGB image; (b) Edge map obtained through the Canny edge detector; (c) Edge map after removing some false positives edge segments; (d) Determination of the normalized mean intensity difference between the peripheral regions; (e) Initial snake points finding process; and (f) Initial snake curve.

of the relative importance of each edge. The underlying assumption is that this difference is larger in the edges of the skin lesion. Given n edge segments E_i, $i = 1, ..., n$, the measure of the importance of each edge is given by:

$$I_{E_i} = \left| P_{E_{i_1}} - P_{E_{i_2}} \right| \tag{4.30}$$

where $P_{E_{i_1}}$ and $P_{E_{i_2}}$ are the mean intensities of the peripheral regions. The maximal mean intensity difference is used to normalize I_{E_i}, thus yielding:

$$\overline{I_{E_i}} = \frac{I_{E_i}}{\max_i I_{E_i}} \tag{4.31}$$

Then, every pixel of a given edge E_i is assigned with the value of the respective normalized mean intensity difference between the peripheral regions $\overline{I_{E_i}}$. $\overline{I_{E_i}}$ values range from 0 to 1 and, as expected, the edges of the skin lesion have the highest $\overline{I_{E_i}}$ values (Figure 4.16(d)).

(iii) Initial curve determination

In this step the initial curve to be used in the initialization of the GVF method is automatically defined, by first determining a set of initial points which are then connected to form a closed curve. To accomplish this purpose, a number of radial lines R_{θ_j} are drawn from a point within the lesion to the exterior, each of them with a particular orientation $\theta_j \in [0, ..., 2\pi[, \ j = 1, ..., 16$. The inner point, $C(x_c, y_c)$, is automatically computed through the same procedure used in the region growing method (see subsection 4.2.4.1).

Then, an initial snake point is defined in each radial line R_{θ_j} as follows. First, take the intersection of this line with the edges E_i, $i = 1, ..., n$. Let $P_{R_{\theta_j}}$ be the set of all edge points detected along the radial line R_{θ_j}, i.e., $P_{R_{\theta_j}} = \left\{p_j^1, ..., p_j^{N_j}\right\}$ and let $Q_{R_{\theta_j}} = \left\{q_j^1, ..., q_j^{N_j}\right\}$ be the set of values of the mean intensity difference between peripheral regions, $\overline{I_E}$, associated to each edge point p_j^k, $k = 1, ..., N_j$. Then a subset $S_{R_{\theta_j}}$ of $P_{R_{\theta_j}}$ containing the edge points with highest $Q_{R_{\theta_j}}$ values, is defined as:

$$S_{R_{\theta_j}} = \left\{p_j^k \mid q_j^* - q_j^k \le T_E\right\} \tag{4.32}$$

where

$$q_j^* = \max_{k=1,...,Nj} q_j^k \tag{4.33}$$

and T_E is a predefined threshold value. If $S_{R_{\theta_j}}$ only has one element, then this point is defined as the initial snake point, s_j, along the radial line R_{θ_j}. In case there are more than one point in the subset $S_{R_{\theta_j}}$, the initial snake point is the point s_j^* whose distance to the inner point C is larger, provided that the distance between s_j^* and the point p_j^*, corresponding to the maximum value q_j^*, is not larger than a certain threshold T_d. Figure 4.16(e) illustrates the detection process of the initial snake points positions.

It is important to note that when a given radial line R_{θ_j} does not intersect any edge ($P_{R_{\theta_j}} = \emptyset$), no initial snake point is defined in that line.

After detecting the initial snake points s_j, a curve is obtained using a linear interpolation of these points. Finally, in order to obtain the initial snake curve, this curve is uniformly expanded in all outward directions by 20 pixels to ensure that it contains the skin lesion (Figure 4.16(f)).

Figure 4.17 illustrates the robustness of the automatic snake initialization method, since it works well even in dermoscopic images with a large amount of hairs, in images with fragmented skin lesions, and also in images with skin lesions with different colors and textures. Furthermore, the final segmentation result is achieved after few iterations, since the initial snake curves are in

general placed very close to the skin lesion boundaries.
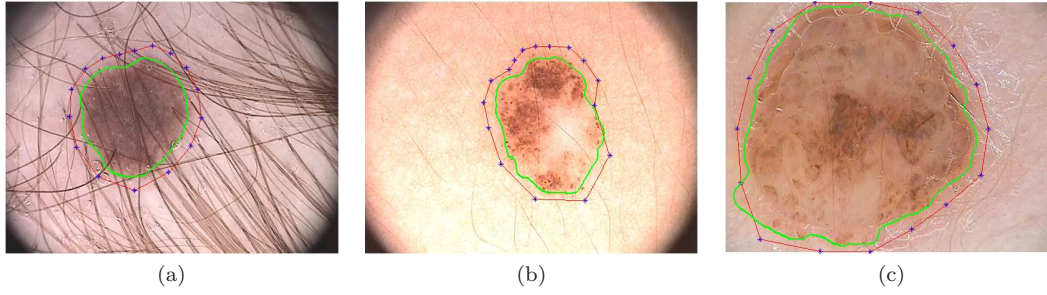
Figure 4.17: GVF snake segmentation in difficult dermoscopic images: (a) Presence of hairs; (b) Fragmented skin lesion; and (c) Skin lesion with multiple colors. In these images the dotted red contour represents the initial snake curve, whereas the green contour corresponds to the final segmentation.

4.2.6 Watershed

Watershed segmentation is a region-based technique that utilizes image morphology. The most intuitive formulation of the watershed transform is based on a flooding simulation. The input grayscale image is considered as an intensity-based topographic surface, in which the bright pixels represent mountaintops and the dark pixels valleys. The aim is to produce the watershed lines on this surface. To accomplish this purpose, holes are punched at each regional minimum in the image, and then the entire topography is flooded from below by allowing water to rise through the holes at a uniform rate. When the rising water coming from two distinct minima is about to merge, a dam is built to prevent the merging. The flooding will eventually reach a stage when only the tops of the dams are visible above the water surface. These dams correspond to the watershed lines, and also to the boundaries of image objects. The final segmented regions arising from the various regional minima are called catchment basins [34, 53, 54]. The flooding process is illustrated in Figure 4.18 for a unidimensional signal.
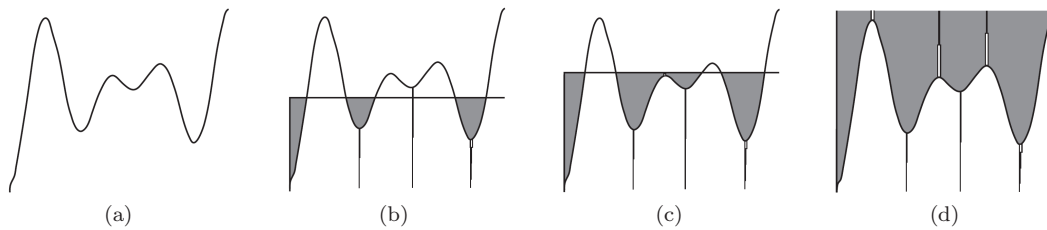
Figure 4.18: Flooding simulation of the watershed transform: (a) Input signal; (b) Punched holes; (c) Dam creation; and (d) Final flooding (Adapted from [34]).

In practice, watershed segmentation is often applied to the gradient of an image, rather than to the image itself. In this formulation, the regional minima of catchment basins correlate nicely with the small value of the gradient corresponding to the objects of interest. Since real digitized images present many regional minima in their gradients, this typically results in an excessive

number of catchment basins (regions), also called oversegmentation. Therefore, pre-processing and/or post-processing phases are usually used to overcome this problem. The pre-processing step is used to filter the image in order to reduce the number of regional minima, creating fewer catchment basins. The post-processing step is applied after the watershed transform for merging the less significant regions in order to obtain larger regions with better correspondence to the objects of interest [34, 53, 61].

4.2.6.1 Implementation

For dermoscopic image segmentation, the watershed transform is applied to the magnitude of the image gradient. However, as gradients of dermoscopic images usually present many regional minima, the result is an oversegmentation of the skin lesion (Figure 4.19). Therefore, a merging procedure is required to overcome this problem.

<div align="center">(a)   (b)   (c)</div>
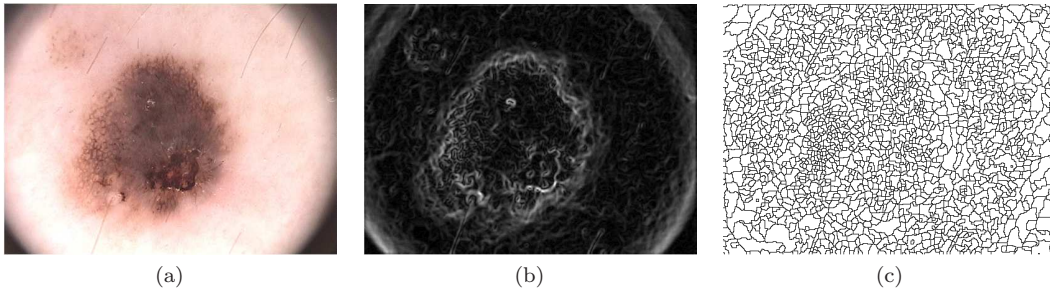
Figure 4.19: Watershed segmentation: (a) Original RGB image; (b) Magnitude of the image gradient; and (c) Watershed segmentation result - oversegmentation.

After applying the watershed transform, the watershed objects are merged based on the histogram of their mean intensities (Figure 4.20). The initial snake curve used in the automatic initialization of the GVF snake method (previously described in subsection 4.2.5.1) is also employed in the merging procedure. The mean intensity level of the initial snake curve mask, L_{begin}, is used to start the merging procedure, and its area is used to obtain an estimation of the skin lesion area, $A_{estimated}$. This area is used in the definition of the stopping criterion for the merging process described next.

Therefore, the merging procedure starts at the gray-level L_{begin} of the watershed object histogram. Then, the watershed objects are iteratively merged until a stopping condition is achieved. The stopping condition depends both on the estimated lesion area, $A_{estimated}$, and on the mean intensity of the watershed objects, more concretely:

$$0.8 \cdot A_{estimated} < A_{merged} < 1.2 \cdot A_{estimated} \quad \wedge \quad |I_{merged} - I_{objects}| > T_s \qquad (4.34)$$

where A_{merged} and I_{merged} are the area and the mean intensity of the current merged region respectively, $I_{objects}$ is the mean intensity of the watershed objects that are about to be merged,

and T_s is a predefined threshold value. The merging procedure stops if the area of the current merged region, A_{merged}, is within $\pm 20\%$ of $A_{estimated}$ (this interval was empirically defined based on the available data to compensate the area estimation errors), and if the difference between the mean intensity of the merged region and the next watershed objects is larger than T_s. Figure 4.20 shows the watershed object merging procedure as well as the final segmentation result after object merging for a given image.
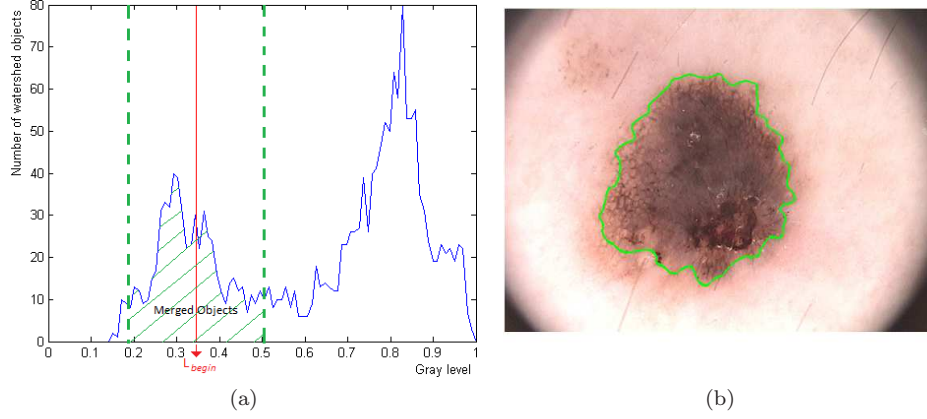
Figure 4.20: Merging procedure: (a) Watershed object histogram; (b) Watershed segmentation result after object merging.

4.3 Post-processing

Most of the implemented segmentation methods require the usage of a set of post-processing operations in order to obtain the final skin lesion segmentation. In general, the post-processing operations are applied to keep the largest binary object from the image, to join small adjacent regions, to fill interior holes, and to smooth the contours (Figure 4.21). These post-processing operations are described below.

Some skin lesions have a great variety of intensities and, sometimes, the segmentation algorithms do not consider some inside regions as belonging to the lesion, which creates some holes within the binary regions. Therefore, a morphological algorithm for region filling is used to fill the interior holes of the binary objects, as shown in Figure 4.21(b).

Besides the skin lesion, the binary image produced by the segmentation methods may also contain other binary regions that have intensities similar to the lesion intensities, such as small isolated islands that belong to the skin, and the regions in the four corners of the image. Therefore, the binary regions corresponding to the dark corners of the image are first eliminated, making use of the corner mask created in the pre-processing step (see subsection 4.1.3). Then, to remove the small isolated islands the largest binary component of the image is selected and assumed to be the lesion (Figure 4.21(b)).

Usually, the segmentation methods produce regions with ragged boundaries. This can be
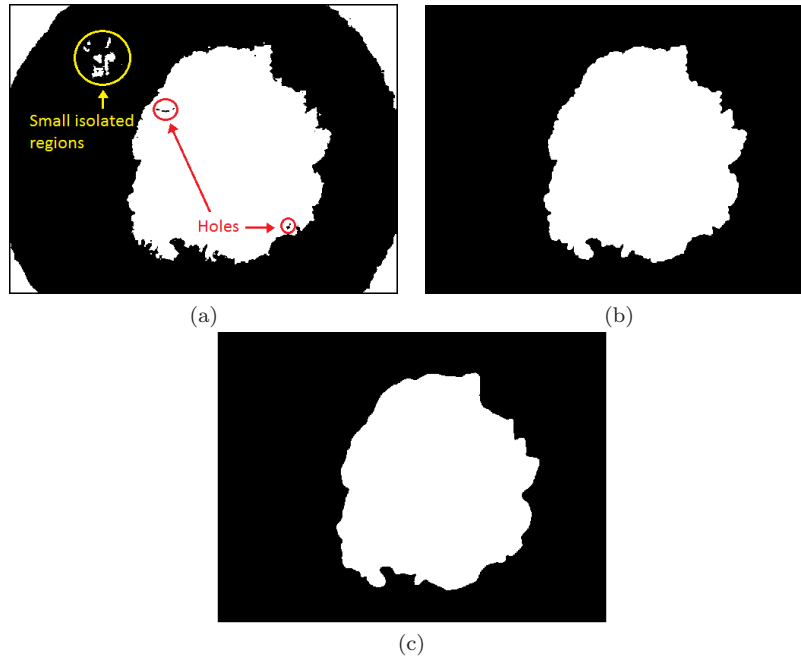
Figure 4.21: Post-processing: (a) Initial segmented image; (b) Segmented image after holes filling, removing of the regions in the four corners, and elimination of the small isolated regions; and (c) Final segmentation result after boundary smoothing.

overcome by smoothing the boundary using either a convolution filter or a curve fitting procedure. A simple yet effective smoothing operation is the convolution of the input boundary with a moving average filter, also known as a box filter [34]:

$$B_{output}(i) = \frac{1}{W} \sum_{j=-(W-1)/2}^{(W-1)/2} B_{input}(i-j) \tag{4.35}$$

where B_{input} is the input boundary coordinates, B_{output} is output boundary coordinates, and W is the filtering degree. This smoothing operation turns the boundary of the lesion more similar to the result of manual segmentation by a dermatologist, and produces a visually satisfactory final segmentation result (Figure 4.21(c)).

4.4 Experimental results

The implemented segmentation algorithms were evaluated on a set of 46 images obtained from the Hospital Pedro Hispano database, including different kinds of dermoscopic images, such as benign melanocytic nevi and melanomas. These are 8-bit RGB color images with dimensions 768×560 pixels.

The manual segmentation of the dermoscopic images to be used as ground truth in the evaluation of the segmentation methods was performed by an expert dermatologist. Three performance metrics are used for the quantitative assessment of the segmentation differences between the manual segmentation (GT) and the output of the automatic segmentation methods (AS).

56

These metrics are the Hammoude distance (HM), the false negative rate (FNR), and the false positive rate (FPR).

The Hammoude distance is based on a comparison of the differences between two boundaries, and is defined as:

$$HM = \frac{\#(AS \cup GT) - \#(AS \cap GT)}{\#(AS \cup GT)} \tag{4.36}$$

This metric takes into account two different types of error, corresponding to the false negatives and the false positives, giving the same importance to both of them. Therefore, besides the Hammoude distance, two separate metrics are used to take into account the two types of error individually [9].

FNR metric measures the rate of pixels classified as lesion by the medical expert that were not classified as lesion by the automatic segmentation:

$$FNR = \frac{\#(\overline{AS} \cap GT)}{\#GT} \tag{4.37}$$

FPR metric measures the rate of pixels classified as lesion by the automatic segmentation algorithm that were not classified as lesion by the medical expert, and can be defined as [9]:

$$FPR = \frac{\#(AS \cap \overline{GT})}{\#GT} \tag{4.38}$$

Table 4.1 shows the median of the performance metrics for the six implemented segmentation methods as well as the percentage of gross errors. The percentage of gross errors is the rate of segmented images with a Hammoude distance greater than 30%, which corresponds to unacceptable segmentation results. This way, the percentage of gross errors can be considered as a measure of the segmentation methods robustness. The GVF snake method is more robust than the other segmentation methods, since it has the smallest percentage of gross errors (2%).

Table 4.1: Results of the segmentation methods.

Segmentation method	HM(%)	FPR(%)	FNR(%)	Gross errors(%)
Automatic thresholding	12.58	6.16	2.05	11
K-means	11.20	5.38	2.19	11
Mean shift	10.65	4.21	3.82	7
Region growing	10.35	4.43	3.68	4
GVF snakes	10.14	3.79	2.85	2
Watershed	12.36	2.70	5.77	7

The best segmentation results according to the Hammoude distance are achieved by the GVF snake method (10.14%). The best false positive rate is obtained by the watershed method with a rate of 2.70%. Automatic thresholding and k-means have the best false negative rate with

a score of 2.05% and 2.19%, respectively. However, both of them have the worst false positive rate among the implemented segmentation methods. This means that automatic thresholding and k-means have a greater tendency to classify some pixels as lesion that were not classified as lesion in the manual segmentation, and thus the automatic segmented boundary lies commonly outside the manual boundary. The GVF snake method provides the best trade-off between false positives (3.79%) and false negatives (2.85%).

Therefore, analyzing the three performance metrics together the GVF snake method can be considered as the best segmentation method, since it has the best Hammoude distance rate, the lowest percentage of gross segmentation errors, and also the best compromise between the false positive rate and the false negative rate.

In general, all implemented segmentation methods provide acceptable results for the majority of the tested images. Figure 4.22 illustrates three examples for which the implemented segmentation methods provide successful skin lesion segmentations. In these dermoscopic images there is a good contrast between the lesion and the surrounding skin, and hence the segmentations results are close to the ground truth segmentation. Furthermore, as the pre-processing step performs a significant hair removal, all the methods often provide good segmentation results even in the images with a large amount of hairs (see dermoscopic image in the third column of Figure 4.22).

Figure 4.23 shows more difficult segmentation cases. There are three main groups of images in which most of the segmentation methods demonstrate limitations and often the skin lesion is not correctly segmented.

One group corresponds to the images in which the lesion is fragmented. The fragmented skin lesion in the first column of Figure 4.23 is only correctly segmented by the GVF snake method. In this case, automatic thresholding as well as the clustering-based methods (k-means and mean shift) first segment the lesion into multiple regions, but as they are spatially separated only the largest region is assumed as lesion. The region-based methods (i.e. region growing) produce a similar final result, since the seed is defined inside the largest fragmented region.

The second group corresponds to the lesions with a great variety of colors and textures. The dermoscopic image in the second column of Figure 4.23 is an example of this kind of lesion, which contains several regions with different colors and properties. In addition, the bottom region of this lesion has a similar intensity to the skin intensity, and because of that most of the implemented segmentation methods produce an unsuccessful segmentation result. This image is only acceptably segmented by the GVF snake and region growing methods.

The third group corresponds to the dermoscopic images where there is a very low contrast, and a smooth transition between the lesion and the skin. An example of this kind of lesion is shown in the third column of Figure 4.23. In this particular image, only the GVF snake method provides

(a) Ground truth   (b) Ground truth   (c) Ground truth

(d) Thresholding   (e) Thresholding   (f) Thresholding

(g) *k*-means   (h) *k*-means   (i) *k*-means

(j) Mean shift   (k) Mean shift   (l) Mean shift

(m) GVF   (n) GVF   (o) GVF

(p) Region growing   (q) Region growing   (r) Region growing

(s) Watershed   (t) Watershed   (u) Watershed
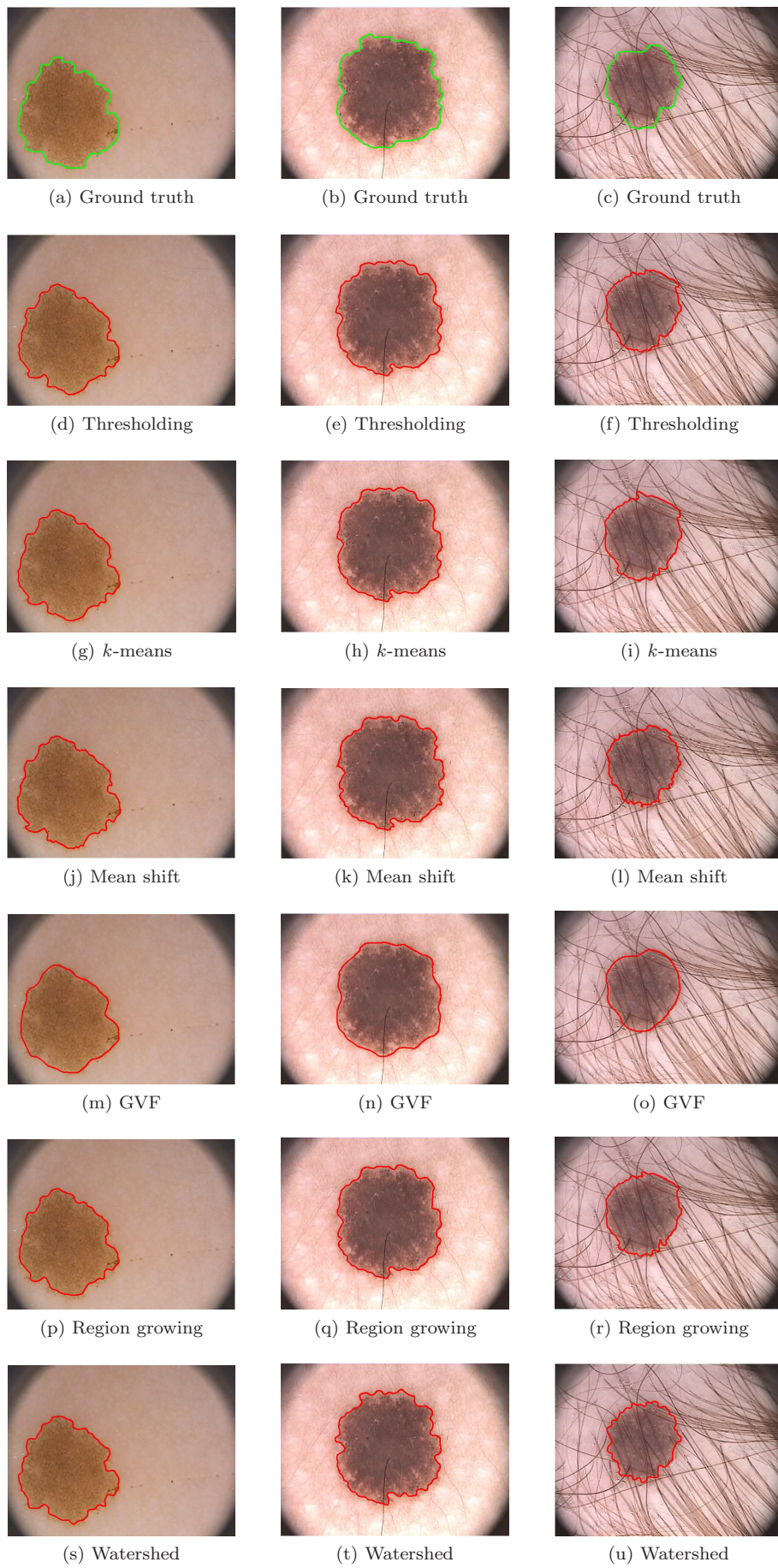
Figure 4.22: Three examples of successful segmentations. In these cases the segmentations results are close to the ground truth segmentation.

(a) Ground truth   (b) Ground truth   (c) Ground truth

(d) Thresholding   (e) Thresholding   (f) Thresholding

(g) k-means   (h) k-means   (i) k-means

(j) Mean shift   (k) Mean shift   (l) Mean shift

(m) GVF   (n) GVF   (o) GVF

(p) Region growing   (q) Region growing   (r) Region growing

(s) Watershed   (t) Watershed   (u) Watershed
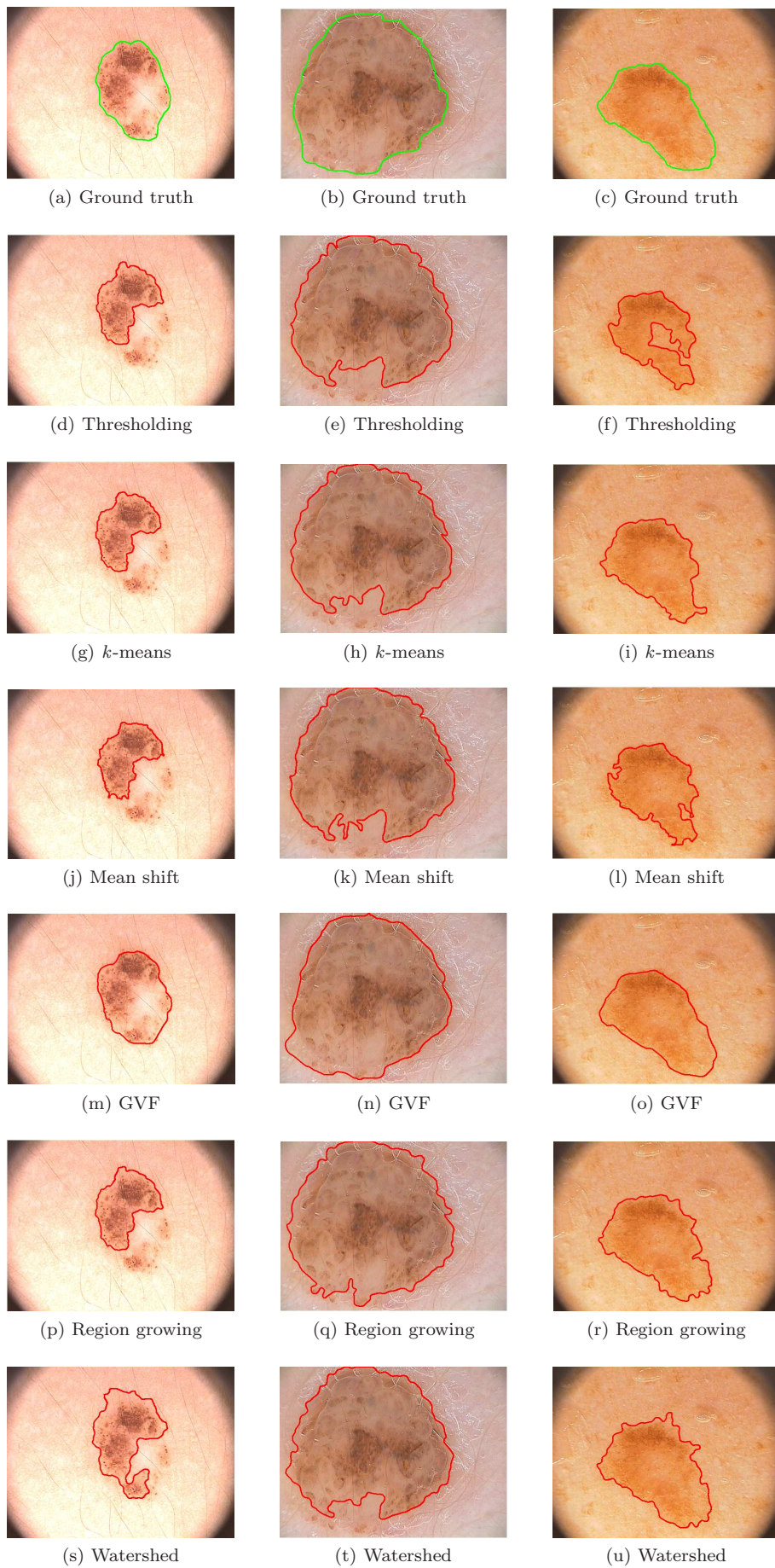
Figure 4.23: Three examples of more difficult segmentation cases.

a successful segmentation result. However, the segmentations provided by other methods (such as region growing and watershed) can be considered acceptable, but with a segmentation error greater than the one obtained by GVF snake method.

In this work, an individually quantitative evaluation for different types of skin lesions is not presented, since the histological classification of the skin lesions is not available for the majority of the images of our dataset. However, based on the available histological classifications it was possible to observe that, in general, the performance of the segmentation methods is better in benign melanocytic lesions than in melanomas. This happens because the dermoscopic structures have an atypical and asymmetrical distribution in melanomas, and hence this kind of lesions often have different colors and textures inside. Furthermore, the boundaries of melanomas are more irregular compared to benign melanocytic lesions, which may vary from very sharp to very fuzzy.

It is important to note that the six implemented segmentation methods are unsupervised, and thus all algorithms perform the lesion segmentation without user intervention, or any kind of initialization.

The segmentation methods were implemented in MATLAB, using a 2.20 GHz and 6 GB RAM computer. Table 4.2 shows the average execution times per image of all implemented segmentation methods. Automatic thresholding is the fastest algorithm (it takes in average 4 s per image) whereas watershed is the slowest algorithm (it takes in average 51 s per image).

Table 4.2: Execution times of the segmentation methods.

Segmentation method	Execution time (s)
Automatic thresholding	4
K-means	8
Mean shift	26
Region growing	9
GVF snakes	44
Watershed	51

Chapter 5

Conclusions and future work

5.1 Conclusions

This dissertation is focused on the manual segmentation/ground truth creation issue as well as on the implementation of fully automated algorithms for the segmentation of dermoscopic images.

Therefore, an annotation tool for manual segmentation and ground truth creation of dermoscopic images is proposed. The annotation tool, called DerMAT, was developed based on the suggestions and requirements of dermatologists, and have already been used by them for ground truth generation. Based on the feedback of the dermatologists, DerMAT has a user friendly graphical interface, and can be considered as an useful and valuable tool since it makes the task of ground truth generation easier and practicable for dermatologists. Furthermore, a functional evaluation of the developed tool was made, based on a comparison with other existing tools that can be also used for ground truth generation. According to this analysis, DerMAT proved to have some advantages with respect to other tools, namely better freehand drawing and reshaping capabilities.

Moreover, a wide spread of algorithms for the automatic segmentation of dermoscopic images were implemented and evaluated, including the automatic thresholding, region growing, watershed, k-means, mean-shift, and GVF snakes. For some of these methods adaptations were made in order to improve their performance and/or make the segmentation process completely automatic. For instance, an automated initialization procedure for the GVF snake method and another for the region growing method are proposed.

A set of different metrics were used in the quantitative assessment of the segmentation performance, namely the Hammoude distance, the false negative rate, and the false positive rate. In general, the results obtained for the 46 dermoscopic images can be considered satisfactory, since for the majority of the tested images the segmentations results are close to the ground truth segmentation. Among the implemented segmentation methods, the GVF snake method achieved

the best segmentation performance, since it had the best Hammoude distance rate (10.14%),the lowest percentage of gross segmentation errors (2%), and also the best trade-off between the false positive rate (3.79%) and the false negative rate (2.85%). These reults show that the GVF snake method is useful and robust enough to be used for the skin lesion segmentation in a computer-aided diagnosis system.

5.2   Future work

As future work, a larger and improved ground truth dataset will be created using DerMAT, containing the histological classification of the skin lesions along with the most relevant dermoscopic structures identification as well as the manual segmentations performed by different dermatologists. The implemented segmentation methods were tested in a ground truth dataset of 46 dermoscopic images, and hence a larger dataset should be used to analyze the reproducibility of the obtained results. The histological classification of the skin lesions is required, in order to evaluate the performance of the segmentation algorithms for different types of skin lesions individually. As the manual segmentation of the skin lesions can be quite subjective, the collection of manual segmentations performed by more than one dermatologist is an important issue, specially to evaluate the inter-rater variability.

Furthermore, automatic segmentation and classification methods will be integrated in DerMAT, since this tool will be an integral part of a final computer-aided diagnosis system of digital dermoscopic images.

Bibliography

[1] "Associação portuguesa de cancro cutâneo." [ONLINE]. Available at: `http://www.apcc.online.pt/`.

[2] G. Argenziano, H. Soyer, V. D. Giorgio, D. Piccolo, P. Carli, M. Delfino, A. Ferrari, R. Hofmann-Wellenhof, D. Massi, G. Mazzocchetti, M. Scalvenzi, and I. H.Wolf, "Dermoscopy, an interactive atlas." EDRA Medical Publishing, 2000. [ONLINE]. Available at: `http://www.dermoscopy.org`.

[3] A. Bonoa, C. Bartolib, N. Cascinellic, M. Lualdid, A. Maurichia, D. Mogliaa, G. Tragnie, S. Tomatisd, and R. Marchesinid, "Melanoma detection. a prospective study comparing diagnosis with the naked eye, dermatoscopy and telespectrophotometry," *Dermatology*, vol. 205, no. 4, pp. 362–366, 2002.

[4] T. M. Deserno, *Biomedical Image Processing (Biological and Medical Physics, Biomedical Engineering)*. Springer, March 2011.

[5] G. C. do Carmo and M. R. e Silva, "Dermoscopy: basic concepts," *International Journal of Dermatology*, vol. 47, pp. 712–719, July 2008.

[6] M. E. Vestergaard, P. Macaskill, P. E. Holt, and S. W. Menzies, "Dermoscopy compared with naked eye examination for the diagnosis of primary melanoma: a meta-analysis of studies performed in a clinical setting," *British Journal of Dermatology*, vol. 159, pp. 669–676, September 2008.

[7] H. Kittler, H. Pehamberger, K. Wolff, and M. Binder, "Diagnostic accuracy of dermoscopy," *The Lancet Oncology*, vol. 3, pp. 159–65, March 2002.

[8] R. P. Braun, L. E. French, and J. H. Saurat, "Dermoscopy of pigmented lesions: a valuable tool in the diagnosis of melanoma," *Swiss Med Wkly*, vol. 134, pp. 83–90, 2004.

[9] M. Silveira, J. C. Nascimento, J. S. Marques, A. R. S. Marçal, T. Mendonça, S. Yamauchi, J. Maeda, and J. Rozeira, "Comparison of segmentation methods for melanoma diagnosis in

dermoscopy images," *IEEE Journal of Selected Topics in Signal Processing*, vol. 3, pp. 35–45, February 2009.

[10] M. E. Celebi, G. Schaefer, H. Iyatomi, and W. V. Stoecker, "Lesion border detection in dermoscopy images," *Computerized Medical Imaging and Graphics*, vol. 33, pp. 148–153, March 2009.

[11] P. M. Ferreira, T. Mendonça, P. Rocha, and J. Rozeira, "An annotation tool for dermoscopic image segmentation," *In Proceedings of the First International Workshop on Visual Interfaces for Ground Truth Collection in Computer Vision Applications: VIGTA*, May 2012.

[12] P. M. Ferreira, T. Mendonça, P. Rocha, and J. Rozeira, "An interactive matlab interface for manual dermoscopic image analysis," *In Proceedings of the 17th Portuguese Conference on Pattern Recognition: RecPad*, October 2011.

[13] P. M. Ferreira, T. Mendonça, P. Rocha, and J. Rozeira, "A new interface for manual segmentation of dermoscopic images," *In Proceedings of the III ECCOMAS Thematic Conference on Computational Vision and Medical Image Processing: VipImage*, October 2011.

[14] "Imagej." [ONLINE]. Available at: http://rsbweb.nih.gov/ij/.

[15] B. Russell, A. Torralba, and W. T. Freeman, "Labelme: The open annotation tool." [ONLINE]. Available at: http://labelme.csail.mit.edu/.

[16] V. Botta, "Annotor." [ONLINE]. Available at: http://www.montefiore.ulg.ac.be/~botta/annotor/index.html.

[17] T. J. Collins, "Imagej for microscopy," *BioTechniques*, vol. 43, pp. S25–S30, July 2007.

[18] B. C. Russell, A. Torralba, K. P. Murphy, and W. T. Freeman, "Labelme: a database and web-based tool for image annotation," *International Journal of Computer Vision*, vol. 77, pp. 157–173, May 2008.

[19] A. Torralba, B. C. Russell, and J. Yuen, "Labelme: online image annotation and applications," *Proceedings of the IEEE*, vol. 98, pp. 1467–1484, August 2010.

[20] "Endrov." [ONLINE]. Available at: http://www.endrov.net/wiki/index.php?title=Main_Page.

[21] "Mango (multi-image analysis gui)." [ONLINE]. Available at: http://ric.uthscsa.edu/mango/.

[22] "Freesurfer." [ONLINE]. Available at: http://surfer.nmr.mgh.harvard.edu/.

[23] P. Pagadala, "Tumor border detection in epiluminescence microscopy images," Master's thesis, Department of Electrical and Computer Engineering, University of Missouri-Rolla, 1998.

[24] M. E. Celebi, S. Hwang, H. Iyatomi, and G. Schaefer, "Robust border detection in dermoscopy images using threshold fusion," *Proceedings of IEEE International Conference on Image Processing*, pp. 2541–2544, September 2010.

[25] L.-K. Huang and M.-J. J. Wang, "Image thresholding by minimizing the measures of fuzziness," *Pattern Recognition*, vol. 28, no. 1, pp. 41–51, 1995.

[26] J. N. Kapur, P. K. Sahoo, and A. K. C. Wong, "A new method for gray-level picture thresholding using the entropy of the histogram," *Computer Vision, Graphics, and Image Processing*, vol. 29, pp. 273–285, March 1985.

[27] J. Kittler and J. Illingworth, "Minimum error thresholding," *Pattern Recognition*, vol. 19, no. 1, pp. 41–47, 1986.

[28] N. Otsu, "A threshold selection method from gray-level histograms," *IEEE Transactions on Systems, Man and Cybernetics*, vol. 9, pp. 62–66, January 1979.

[29] J. Humayun, A. S. Malik, and N. Kamel, "Multilevel thresholding for segmentation of pigmented skin lesions," *Proceedings of IEEE International Conference on Imaging Systems and Techniques*, pp. 310–314, May 2011.

[30] R. B. Dubey, M. Tech, M. Hanmandlu, S. K. Gupta, and S. K. Gupta, "The brain mr image segmentation techniques and use of diagnostic packages," *Academic Radiology*, vol. 17, pp. 658–671, May 2010.

[31] M. E. Celebi, Y. A. Aslandogan, and P. R. Bergstresser, "Unsupervised border detection of skin lesion images," *Proceedings of the International Conference on Information Technology: Coding and Computing*, vol. 2, pp. 123–128, April 2005.

[32] M. E. Celebi, H. A. Kingravi, H. Iyatomi, Y. A. Aslandogan, W. V. Stoecker, R. H. Moss, J. M. Malters, J. M. Grichnik, A. A. Marghoob, H. S. Rabinovitz, and S. W. Menzies, "Border detection in dermoscopy images using statistical region merging," *Skin Research and Technology*, vol. 14, pp. 347–353, August 2008.

[33] H. Wang, X. Chen, R. H. Moss, R. J. Stanley, W. V. Stoecker, M. E. Celebi, T. M. Szalapski, J. M. Malters, J. M. Grichnik, A. A. Marghoob, H. S. Rabinovitz, and S. W. Menzies, "Watershed segmentation of dermoscopy images using a watershed technique," *Skin Research and Technology*, vol. 16, pp. 378–384, August 2010.

[34] Q. Wu, F. Merchant, and K. R. Castleman, *Microscope Image Processing.* Academic Press, 1 ed., April 2008.

[35] D. H. Chung and G. Sapiro, "Segmenting skin lesions with partial-differential-equations-based image processing algorithms," *IEEE Transactions on Medical Imaging*, vol. 19, pp. 763–767, July 2000.

[36] B. Erkol, R. H. Moss, R. J. Stanley, W. V. Stoecker, and E. Hvatum, "Automatic lesion boundary detection in dermoscopy images using gradient vector flow snakes," *Skin Research and Technology*, vol. 11, pp. 17–26, February 2005.

[37] H. Zhou, G. Schaefer, M. E. Celebi, H. Iyatomi, K.-A. Norton, T. Liu, and F. Lin, "Skin lesion segmentation using an improved snake model," *Proceedings of the IEEE Engineering in Medicine and Biology Society*, pp. 1974–1977, 2010.

[38] P. Schmid, "Segmentation of digitized dermatoscopic images by two-dimensional color clustering," *IEEE Transactions on Medical Imaging*, vol. 18, pp. 164–171, February 1999.

[39] D. D. Gómez, C. Butakoff, B. K. Ersboll, and W. Stoecker, "Independent histogram pursuit for segmentation of skin lesions," *IEEE Transactions on Biomedical Engineering*, vol. 55, pp. 157–161, January 2008.

[40] R. Melli, C. Grana, and R. Cucchiara, "Comparison of color clustering algorithms for segmentation of dermatological images," *Proceedings of the SPIE Medical Imaging*, vol. 6144, February 2006.

[41] Y. Zhou, M. Smith, L. Smith, and R. Warr, "Segmentation of clinical lesion images using normalized cut," *Image Analysis for Multimedia Interactive Services*, pp. 101–104, May 2009.

[42] R. S. Devi, L. P. Suresh, and K. L. Shunmuganathan, "Intelligent fussy system based dermoscopic image segmentation for melanoma detection," *International Conference on Sustainable Energy and Intelligent Systems*, pp. 739–743, July 2011.

[43] N. Sharma and L. M. Aggarwal, "Automated medical image segmentation techniques," *Journal of Medical Physics*, vol. 35, pp. 3–14, January 2010.

[44] T. F. Chan, B. Y. Sandberg, and L. A. Vese, "Active contours without edges for vector-valued images," *Journal of Visual Communication and Image Representation*, vol. 11, pp. 130–141, June 2000.

[45] Q. Abbas, M. E. Celebi, I. F. García, and M. Rashid, "Lesion border detection in dermoscopy images using dynamic programming," *Skin Research and Technology*, vol. 17, pp. 91–100, February 2011.

[46] E. L. Psaty and A. C. Halpern, "Current and emerging technologies in melanoma diagnosis: the state of the art," *Clinics in Dermatology*, vol. 27, pp. 35–45, February 2009.

[47] R. P. Braun, H. S. Rabinovitz, M. Oliviero, A. W. Kopf, and J. H. Saurat, "Dermoscopy of pigmented skin lesions," *American Academy of Dermatology*, vol. 55, no. 1, pp. 109–121, 2005.

[48] R. A. Schwartz, *Skin Cancer: Recognition and Management.* Wiley-Blackwell, 2 ed., 2008.

[49] J. Malvehy, S. Puig, R. P. Braun, A. A. Marghoob, and A. W. Kopf, *Handbook of Dermoscopy.* Taylor & Francis, 1 ed., 2006.

[50] R. H. Johr, "Dermoscopy: Alternative melanocytic algorithms - the abcd rule of dermatoscopy, menzies scoring method, and 7-point checklist," *Clinics in Dermatology*, vol. 20, no. 3, pp. 240–247, 2002.

[51] "Addi project." [ONLINE]. Available at: http://www2.fc.up.pt/addi/.

[52] X. Li, B. Aldridge, R. Fisher, and J. Rees, "Estimating the ground truth from multiple individual segmentations incorporating prior pattern analysis with application to skin lesion segmentation," *Proceedings of 8th International Symposium on Biomedical Imaging*, pp. 1438–1441, April 2011.

[53] R. C. Gonzalez and R. E. Woods, *Digital image processing.* Upper Saddle River: Prentice Hal, 2 ed., 2002.

[54] I. N. Bankman, *Handbook of medical imaging: processing and analysis.* Academic Press, 1 ed., 2000.

[55] Q. Abbas, M. E. Celebi, and I. F. Garciá, "Hair removal methods: A comparative study for dermoscopy images," *Biomedical Signal Processing and Control*, vol. 6, no. 4, pp. 395–404, 2011.

[56] C. Barata, J. S. Marques, and J. Rozeira, "Detecting the pigment network in dermoscopy images: a directional approach," *International Conference of the IEEE Engineering in Medicine and Biology Society*, pp. 5120–5123, 2011.

[57] M. Bertalmio, G. Sapiro, V. Caselles, and C. Ballester, "Image inpainting," *Proceedings of SIGGRAPH*, pp. 417–424, 2000.

[58] S. Y. Park and Y. H. Lee, "Double smoothing of images using median and wiener filters," *IEEE Transactions on Acoustics, Speech and Signal Processing*, vol. 37, no. 6, 1989.

[59] R. C. Gonzalez and R. E. Woods, *Digital image processing.* Upper Saddle River: Prentice Hal, 2 ed., 2002.

[60] M. Sonka, V. Hlavac, and R. Boyle, *Image Processing, Analysis, and Machine Vision.* Thomson, 3 ed., 2008.

[61] F. Monteiro, *Region-based spatial and temporal image segmentation.* PhD thesis, Faculdade de Engenharia da Universidade do Porto, 2007.

[62] S. Lakare, *3D Segmentation Techniques for Medical Volumes.* 2000.

[63] M. Sezgin and B. Sankur, "Survey over image thresholding techniques and quantitative performance evaluation," *Journal of Electronic Imaging*, vol. 13, no. 1, pp. 146–168, 2004.

[64] M. S. Nixon and A. S. Aguado, *Feature extraction and image processing.* Oxford: Newnes, 1 ed., 2002.

[65] X. Xu, S. Xu, L. Jin, and E. Song, "Characteristic analysis of otsu threshold and its applications," *Pattern Recognition Letters*, vol. 32, pp. 956–961, 2011.

[66] U. Gonzales-Barron and F. Butler, "A comparison of seven thresholding techniques with the k-means clustering algorithm for measurement of bread-crumb features by digital image analysis," *Journal of Food Engineering*, vol. 74, no. 2, pp. 268–278, 2006.

[67] R. Rocha, *Image segmentation and reconstruction of 3D surfaces from carotid ultrasound images.* PhD thesis, Faculdade de Engenharia da Universidade do Porto, 2007.

[68] G. W. Zack, W. E. Rogers, and S. A. Latt, "Automatic measurement of sister chromatid exchange frequency," *Journal of Histochemistry and Cytochemistry*, vol. 25, no. 7, pp. 741–753, 1977.

[69] A. Likas, N. Vlassis, and J. J. Verbeek, "The global k-means clustering algorithm," *Pattern Recognition 36*, vol. 36, no. 2, pp. 451–461, 2003.

[70] P. Quelhas, *Scene Image Classification and Segmentation with Quantized Local Descriptors and Latent Aspect Modeling.* PhD thesis, EPFL, 2006.

[71] J. S. Suri, D. L. Wilson, and S. Laxminarayan, *Handbook of Biomedical Image Analysis - Volume II: Segmentation Models Part B.* Kluwer Academic/Plenum Publishers, 2005.

[72] J. S. Suri, D. L. Wilson, and S. Laxminarayan, *Handbook of Biomedical Image Analysis - Volume I: Segmentation Models Part A.* Kluwer Academic/Plenum Publishers, 2005.

[73] W. Fei and S. Zhu, "Mean shift clustering-based moving object segmentation in the h.264 compressed domain," *IET Image Processing*, vol. 4, no. 1, pp. 11–18, 2010.

[74] C. Xu and J. L. Prince, "Snakes, shapes, and gradient vector flow," *IEEE Transaction on image processing*, vol. 17, no. 3, 1998.

[75] M. Kass, A. Witkin, and D. Terzopoulos, "Snakes: Active contour models," *International Journal Computer Vision*, pp. 321–331, 1988.

[76] J. Canny, "A computational approach to edge detection," *IEEE Transactions on Pattern Analysis and Machine Intelligence*, vol. 8, no. 6, pp. 679–714, 1986.

[77] C. Kamath, *Scientific Data Mining: A Practical Perspective.* Society for Industrial and Applied Mathematics, 2009.

[78] L. S. Davis, "A survey of edge detection techniques," *Computer Graphics and Image Processing*, vol. 4, pp. 248–270, 1975.